CANCER

Multi-armored allogeneic MUC1 CAR T cells enhance efficacy and safety in triple-negative breast cancer

Piril Erler[1], Tomasz Kurcon[1], Hana Cho[1], Jordan Skinner[1], Chantel Dixon[1], Steven Grudman[1], Sandra Rozlan[2], Emilie Dessez[2], Ben Mumford[1], Sumin Jo[1], Alex Boyne[1], Alexandre Juillerat[1], Philippe Duchateau[2], Laurent Poirot[2], Beatriz Aranda-Orgilles[1]*

Solid tumors, such as triple-negative breast cancer (TNBC), are biologically complex due to cellular heterogeneity, lack of tumor-specific antigens, and an immunosuppressive tumor microenvironment (TME). These challenges restrain chimeric antigen receptor (CAR) T cell efficacy, underlining the importance of armoring. In solid cancers, a localized tumor mass allows alternative administration routes, such as intratumoral delivery with the potential to improve efficacy and safety but may compromise metastatic-site treatment. Using a multi-layered CAR T cell engineering strategy that allowed a synergy between attributes, we show enhanced cytotoxic activity of MUC1 CAR T cells armored with PD1^{KO}, tumor-specific interleukin-12 release, and TGFBR2^{KO} attributes catered towards the TNBC TME. Intratumoral treatment effectively reduced distant tumors, suggesting retention of antigen-recognition benefits at metastatic sites. Overall, we provide preclinical evidence of armored non-alloreactive MUC1 CAR T cells greatly reducing high TNBC tumor burden in a TGFB1- and PD-L1–rich TME both at local and distant sites while preserving safety.

INTRODUCTION

Worldwide, breast cancer remains the most common malignancy in women. Among all subtypes, triple-negative breast cancer (TNBC) is noted as the most aggressive with a high metastatic potential and poor survival rates (1). TNBC accounts for 10 to 20% of all breast cancers, and to date, patients have limited therapeutic options due to the lack of targetable hormone receptors in this subtype (2). Despite the emergence of a few recent targeted therapy options that are under investigation [i.e., Poly (ADP-ribose) polymerase (PARP), Phosphatidylinositol-4,5-biphosphate 3-kinase catalytic subunit alpha (PIK3CA), and programmed cell death protein 1 (PD-1) and angiogenesis inhibitors], surgery, chemotherapy, and radiation therapy continue to be the standard of care, and their success remains limited (3, 4). As an alternative, chimeric antigen receptor (CAR) T cell therapies could provide an invaluable option for patients with advance-stage TNBC.

In solid tumors, CAR T cell therapy effectiveness encounters numerous challenges due to the sparse number of tumor-specific antigens, large tumor heterogeneity, a highly immuno-inhibitory tumor microenvironment (TME), ineffective T cell trafficking, and tumor infiltration (5, 6). To overcome these challenges, mounting lines of evidence suggest that CAR T cells require additional functional armoring to boost potency and proliferation while preventing cellular dysfunction (7–11). As a result, in addition to choosing an ideal target antigen and identifying an optimal Single-chain Fragment Variable (scFv), multi-layered gene engineering strategies and alternative administration approaches appear critical to foster the efficacy and safety of CAR T cells against solid tumors.

MUC1 is a heavily glycosylated protein expressed on the apical surface of normal epithelial tissues. Confined to the lumen in normal physiological structures, normal MUC1 antigen is protected from the external environment (12). In contrast, tumor-associated MUC1 is hypo-glycosylated, thereby enabling differential antigenic

recognition with specific scFvs (13, 14). Moreover, tumor-associated MUC1 is overexpressed and losing its polarization, it is dispersed throughout the surface of the tumor cells, increasing the prospect of interacting with cells in the peripheral blood (PB) (15). In TNBC, MUC1 expression is detected in 94% and overexpression is noted in 67% of the patient tumors (16). Because it is also associated with cancer cell stemness (17), and has a high rate of overexpression in a variety of solid cancers, tumor-specific MUC1 represents a valuable target in a large range of solid tumors (15).

Among other immune-evasive mechanisms, the programmed death-ligand 1 (PD-L1)/PD1 and TGFB1-transforming growth factor-B1 (TGFB1)/TGFBR2 axes are some of the key mediators of T cell dysfunction and impaired proliferation deployed in the TME of TNBC and other solid tumors (18, 19). These mechanisms commonly challenge CAR T cells to efficiently mount an antitumor response and to provide optimal CAR T cell expansion, which is crucial for a substantial reduction of the tumor burden (20, 21). Interleukin-12 (IL-12) cytokine is known to increase CAR T cell proliferation, yet its systemic toxicity has been recorded in several models and is preventing its success in the clinic (22, 23). Thus, inducible mechanisms to secrete IL-12 or other cytokines have become paramount to decrease risks associated with systemic toxicity while maintaining the efficacy of the CAR T cells (11, 24–29).

In addition to multiplexed engineering and inducible cytokine release strategies, regional or intratumoral administration of CAR T cells may be used as an alternative to intravenous administration to address challenges associated with tumor trafficking and infiltration, as well as to potentially decrease off-tumor toxicities (30–37). Although there are increasing number of clinical trials investigating intratumoral administration of immunotherapeutic agents, studies applying intratumoral administration of CAR T cells for breast cancer treatment remain limited to date (30, 31, 38–43). Efficient targeting of metastatic sites is crucial for patients with late-stage TNBC because mortality risk increases with metastasis. Since intratumoral administration can confine the CAR T cells to the tumor, it is vital to ensure that this route of administration can still effectively target

---

[1]Cellectis Inc., New York, NY, USA. [2]Cellectis SA, Paris, France.
*Corresponding author. Email: beatriz.aranda-orgilles@cellectis.com

metastatic sites while providing advantages to efficacy. Overall, it is optimal to develop CAR T cells capable of migrating to distant tumor sites while maintaining low levels in circulation for increased safety. Engineering efforts to armor CAR T cells have increased in the last years in the quest to enhance CAR T cell efficacy and trafficking to solid tumors (6, 7, 44, 45). However, highly active armored CAR T cells could pose a toxicity risk; therefore, a combination of intratumoral administration along with CAR T cells armoring strategies is emerging as an attractive avenue to safely and efficiently target solid tumors while reaching distant sites (33, 46).

Herein, we identified an efficient MUC1 scFv with high tumor coverage and investigated its therapeutic potential using in vitro and in vivo assays in TNBC tumor models. To increase efficacy against solid tumors, we generated non-alloreactive MUC1 CAR T cells carrying multiple CAR T cell enhancing attributes edited by Transcription activator-like effector nucleases (TALEN) technology to evaluate whether the combination of attributes confers additional benefits. In detail, we engineered non-alloreactive/universal CAR T cells harboring a *TRAC* knockout to prevent graft versus host disease in an allogeneic context (UCART) and a recombinant lentiviral vector (rLV) to express a second-generation MUC1 CAR (UCARTM1). We further edited the non-alloreactive UCARTM1 with a *PDCD1* and *TGFBR2* TALEN-mediated knockout and inserted IL-12 under the regulatory elements of *PDCD1* allowing its transcription and consecutive secretion to be induced by antigen-mediated CAR T cell activation (UCARTM1$^{\Delta PD1/IL12; \Delta TGFBR2}$) (11). Alongside with intravenous delivery, we evaluated the therapeutic potential of multi-edited CAR T cells used in combination with intratumoral administration in increasing efficacy and safety. Furthermore, we assessed the therapeutic control over TNBC tumors exhibiting an immunosuppressive TME and at distant sites with high tumor burden. In these preclinical models, we also monitored CAR T cell and IL-12 levels systemically to assess the benefits of combining different attributes as well as different delivery routes to reduce the potential off-tumor risks and IL-12–related toxicities to maintain safety. Altogether, our study shows that multi-armored CAR T cells can effectively clear tumors in both intratumoral and intravenous models with a range of CAR T cell dosing and tumor burden while limiting off-tumor toxicities, thus allowing us to consider different approaches for clinical development to balance efficacy and safety.

RESULTS

### In vitro screening identifies lead scFvs for MUC1 CAR T cells

We used several scFvs (M1 to M7) from the literature targeting various regions and glycosylation patterns of tumor-associated MUC1 (table S1) and assembled them into a CAR structure carrying a CD8α hinge and transmembrane domain, a 4-1BB costimulatory domain, and a CD3ζ activation domain (Fig. 1A). Moreover, the CAR constructs carried two CD20 mimotopes (R2) that allow the detection of the CAR with the Food and Drug Administration–approved antibody rituximab (47). We generated lentiviruses with these plasmids and verified their expression in Jurkat and T cells (Fig. 1B and fig. S1A). In parallel, we interrogated the Cancel Cell Line Encyclopedia and previous literature to identify breast cancer cell lines expressing *MUC1* (fig. S1B). Using flow cytometry, we confirmed MUC1 protein expression via flow cytometry using three independent antibodies identifying different forms of the MUC1

antigen with different glycosylation patterns, mostly recognizing the underglycosylated protein (48–51) (table S2, Fig. 1C, and fig. S1C) in eight breast cancer cells lines (T47D, MDA-MB-468, HCC1937, HCC1395, HCC70, HCC38, MDA-MB-231, and MCF7). HCC70, a TNBC cell line, and T47D, an ERα-positive luminal A cell line, showed the highest levels of tumor-associated MUC1 expression (Fig. 1C). To use these cell lines in in vitro and in vivo experiments, we generated HCC70-GFP (green fluorescent protein) and T47D-GFP cell lines with an rLV encoding NanoLuc_T2A_EGFP. We then screened six of the candidate CAR T cells that had shown good CAR expression in T cells, in a cytotoxic assay with T47D-GFP cells (imaged and analyzed with the Incucyte live-cell analysis system) and identified four CAR T cells with high killing efficiency (CARTM1, CARTM2, CARTM3, and CARTM4) when compared to other candidates and the NTD controls (nontransduced; T cells without CAR) (fig. S1D). Furthermore, we evaluated different effector-target cell ratios and confirmed dose-dependent tumor killing of HCC70-GFP and T47D-GFP cells when cocultured with each of these CAR T cells (Fig. 1D). In this assay, we noted that CARTM1, CARTM3, and CARTM4 outperformed CARTM2 with similar efficiencies.

To evaluate whether the selected scFvs are tumor-specific, we produced proteins encoding three of these scFvs (M1, M3, and M4) coupled to the Fc portion of IgG1 and assessed whether they detected MUC1 on primary cell lines from kidney (high expression), lung (high expression), cervical tissues (high expression), and mammary tissues (medium expression) (Human Protein Atlas, proteinatlas.org) (fig. S1, E and F). Flow cytometry analysis showed no binding of any of the scFv proteins or the antibodies tested to the primary epithelial cells while M1 and M3 strongly recognized the MUC1 antigen on two breast cancer cell lines tested, as expected (Fig. 1, E and F, and fig. S1G). We also performed an intracellular staining to confirm that MUC1 is expressed in healthy epithelial cells evaluated, indicating that the pattern of recognition by the scFv is dependent on posttranslational modifications and not exclusively expression (fig. S1H). Finally, we performed a tissue microarray analysis using immunohistochemistry to assess both the ability of the selected scFvs to bind tumor-associated MUC1 in primary tumor samples and their tumor coverage. Ninety-five breast tumor samples, representative of different malignancy stages from IA to IIIC, were included in this array in duplicates. About 95% of the samples showed positive staining with various intensities of staining for the three scFv proteins tested compared to the negative control, and the highest intensity of staining was observed for M1 (Fig. 1G). In sum, upon this initial analysis, we identified at least three MUC1 scFvs with a large interpatient tumor coverage showing no binding to healthy primary cells tested and observed strong cytotoxic activity of CAR T cells engineered with these scFvs in a dose-dependent manner in vitro.

UCARTM1 treatment shows dose-dependent tumor control and extends survival

To evaluate CAR T cells in a more physiologically relevant manner, we established a solid tumor model by orthotopically injecting HCC70-GFP cells in the mammary gland and used it to test CAR T cell activity in vivo at different doses administered intravenously. For the in vivo experiments, we made our CAR T cells non-alloreactive by knocking out the *TRAC* gene (referred to as UCART), thus preventing surface expression of αβTCR, which also helped to exclude any potential confounding activity arising from TCR-mediated allo or
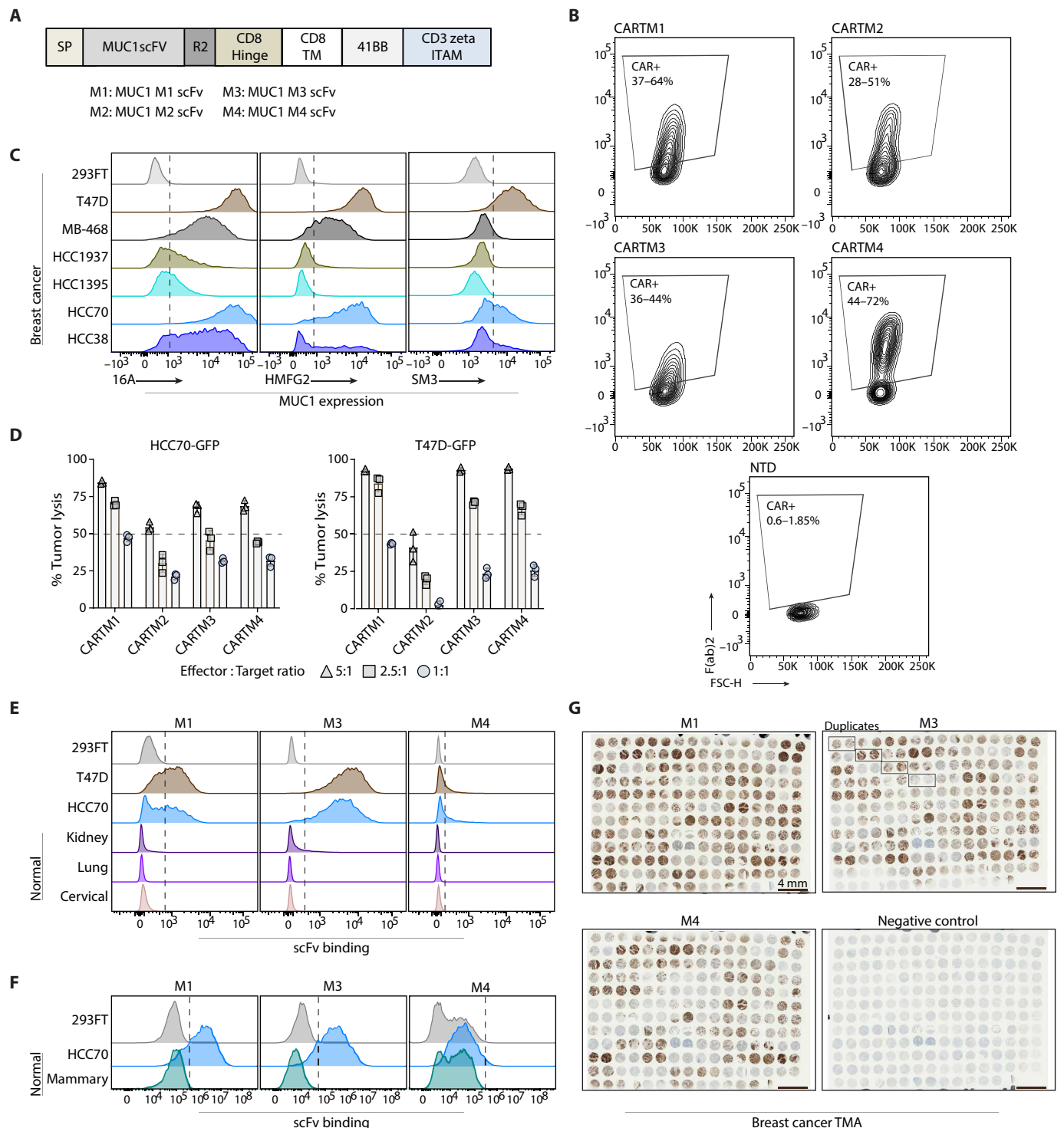
Fig. 1. CAR T cells engineered with tumor-specific MUC1 scFvs show dose-dependent killing in vitro. (**A**) Design of the MUC1 CAR. (**B**) Flow cytometry analysis of CAR expression in T cells. The range is based on percentages observed in different donors ($n = 3$), staining was done with anti-human F(ab')2 or anti-mouse F(ab')2 based on the origin of the scFvs. (**C**) Flow cytometry analysis of MUC1 expression in breast cancer cell lines, with three different antibodies. (**D**) Cytotoxic assay with cocultures set up with different E:T ratios ($n = 3$). Each point represents a technical replicate. (**E**) Flow cytometry detection of MUC1 scFv-derived antibodies binding to healthy lung, kidney, and cervical epithelial primary cells and breast cancer cell lines. (**F**) Flow cytometry detection of MUC1 scFv-derived antibodies binding to healthy mammary epithelial primary cells and the HCC70 breast cancer cell line. (**G**) Tissue microarray IHC staining of breast cancer tumors with MUC1 scFv-derived antibodies and negative control.

xeno response in cellular or in vivo assays (Fig. 2, A and B) (52). All NTD control cells used for the in vivo experiments were also modified with a $TRAC^{KO}$ and TCR depleted to achieve a ~100% TCR^{KO} population (fig. S2A). For the initial dose titration, we used UCARTM1 out of the four CAR T cells engineered with different scFvs as a representative. However, we did not detect efficient tumor reduction regardless of the increased UCARTM1 dose (fig. S2B). Considering that unarmored CAR T cells might exhibit limited activity in solid tumors, we sought to include attributes that may enhance CAR T cell function in vivo to allow the evaluation of different scFvs.

We previously published that CAR T cells carrying a TALEN-mediated PD1 knockout and are capable of secreting IL-12 under the *PDCD1* regulatory elements exhibit enhanced antitumor activity (11). This targeted integration does not allow IL-12 to be expressed at baseline because PD1 is not expressed in resting T cells, while IL-12 can be induced when the T cell is activated upon recognition of tumor antigen by the CAR. In this system, the deltaLNGFR (dLNGFR) surface marker serves as a surrogate marker to trace IL-12 expression as they are both delivered using an IL-12–dLNGFR repair matrix that can then generate two independent proteins via ribosomal skipping mediated by T2A (fig. S2C). To understand whether the $PD1^{KO}$ attribute is also relevant in TNBC, we performed an analysis using The Cancer Genome Atlas (TCGA) database (phs000178) that revealed high *PDCD1* gene expression in the TNBC bulk tumor relative to other breast cancer subtypes (fig. S2D). Similarly, an abundance of $PD1^{+}$ exhausted T cells in TNBC has been described by other groups (53). We also evaluated PD-L1 expression in HCC70-GFP tumors via immunohistochemistry (IHC) staining, validating that our model could recapitulate $PD-L1^{+}$ tumors (fig. S2E). In addition, based on our previous findings and the effects of IL-12 described in the literature, we hypothesized that IL-12 could also boost MUC1 CAR T cell proliferation and contribute to tumor control. Therefore, we armored non-alloreactive MUC1 CAR T cells with *PDCD1* knockout and targeted integration of IL-12 ($UCART^{\Delta PD1/IL12}$), providing tight control under the PD1 regulatory elements of this potent immunoinflammatory cytokine upon antigen encounter, as previously shown (47) (Fig. 2A). This gene editing strategy has multiple benefits as it can provide protection from potential PD-L1–mediated inhibition of CAR T cells and confines the IL-12 release to the tumor site bypassing potential systemic toxic effects (54). We aimed to achieve high $PD1^{KO}$ efficiency but limited the IL-12^{KI} to only a small portion of the edited cells to boost activity while adding another tier of safety to IL-12 use. Figure 2B shows a representative CAR integration around 50% for all the samples evaluated and as IL-12 is only expressed upon activation, we stimulated the cells with phorbol 12-myristate 13-acetate (PMA)/ionomycin and demonstrated expression of the surrogate marker dLNGFR exclusively in the $PD1^{KO}$ cells (Fig. 2C).

To investigate the potential benefits of $PD1^{KO}$ and IL-12 release attribute in this model, we orthotopically injected HCC70-GFP cells and intravenously administered UCARTM1 and $UCARTM1^{\Delta PD1/IL12}$ along with $NTD^{\Delta PD1/IL12}$, NTD, and phosphate-buffered saline (PBS) controls. We observed that animals treated with $UCARTM1^{\Delta PD1/IL12}$ displayed higher tumor control compared to UCARTM1 (fig. S2F). HCC70-GFP tumors resected at 77 days after treatment revealed that while UCARTM1 infiltrated the tumor but failed to control growth, $UCARTM1^{\Delta PD1/IL12}$ showed higher infiltration levels and hence better tumor growth control (Fig. 2, D and E). This was also

reflected in the higher number of immune $hCD45^{+}$ cells identified in the tumor (fig. S2G).

We then used this model to compare the efficacy of the candidate UCARTs engineered with M1, M2, M3, or M4 scFv. Of note, the CAR T cells generated with different scFvs yielded a comparable T cell phenotype profile (fig. S2H). As some CAR T cells can show variability in activity in vitro and in vivo, we included CAR T cells we had engineered with the M2 scFv despite its lower cytotoxic activity in vitro relative to the other candidates. Intravenous treatment of 50-mm^3 HCC70-GFP tumors engrafted orthotopically showed that $UCARTM1^{\Delta PD1/IL12}$, $UCARTM2^{\Delta PD1/IL12}$, and $UCARTM4^{\Delta PD1/IL12}$ perform similarly and clear the tumors in 3 to 4 weeks compared to NTD and PBS control groups (Fig. 2F). $UCARTM3^{\Delta PD1/IL12}$, however, exhibited an interesting pattern exerting tumor control in a delayed manner, effectively reducing the tumor growth at later time points (Fig. 2F). We then focused on two constructions to perform an intravenous dose response study: (i) UCARTM1—given its high intensity staining in the tissue microarray, high tumor killing efficiency both in vitro and in vivo, and selective binding of the scFv to tumor-specific MUC1 antigen; and (ii) UCARTM3—based on its interesting, slower-acting profile in vivo, efficient activity in vitro, and selective binding of the scFv to tumor-specific MUC1 antigen. We observed that while $UCARTM1^{\Delta PD1/IL12}$ showed dose-dependent activity (Fig. 2, G and H), $UCARTM3^{\Delta PD1/IL12}$ was not active at lower doses and displayed variable activity at higher doses (Fig. 2H). However, both $UCARTM1^{\Delta PD1/IL12}$ and $UCARTM3^{\Delta PD1/IL12}$ showed a larger number of $hCD45^{+}$ cells in the tumor in the higher dose cohorts as expected (Fig. 2I). We examined the profile of the T cells in the tumor at day 54 using CD62L, LAG-3, and TIM-3 to evaluate differentiation and exhaustion and observed no notable differences between both scFvs (fig. S2I). The different doses of UCARTM1 administered yielded a different profile displaying a larger number of exhaustion markers with the lower dose, which could explain the reduced in vivo antitumor activity observed. None of the doses tested with either CAR T cell affected animal health and weight during the experiment (fig. S2J). Survival of the animals was also significantly extended upon treatment of either dose of $UCARTM1^{\Delta PD1/IL12}$, but consistent with the heterogeneous tumor-control response, $UCARTM3^{\Delta PD1/IL12}$ did not extend the survival of the mice (Fig. 2J). On the basis of these results, we selected UCARTM1 to further investigate and additionally interrogated whether the location of the tumor had an impact on response to treatment. We compared an orthotopic and a subcutaneous tumor model by treating the cohorts with intravenously administered $UCARTM1^{\Delta PD1/IL12}$ when the tumors reached 50 mm^3 and observed efficient tumor control in both cases compared to NTD and PBS controls (fig. S2K). Altogether, these results confirmed that M1 scFv represents a suitable candidate for the further development of non-alloreactive MUC1 CAR T cells (UCARTM1), as it has strong activity in vitro and in vivo, and the scFv does not bind MUC1-expressing healthy epithelial tissues.

Intratumoral administration increases the efficacy of the UCARTM1 treatment

Our previous experiments showed that UCARTM1 activity was limited when not enhanced with the $PD1^{KO}$/IL-12^{KI} attribute; hence, we wondered whether this was a result of deficient trafficking and infiltration or that the scFv selected failed to elicit a strong antigen-recognition response in vivo. Intratumoral administration has been shown to overcome challenges associated with CAR T cell
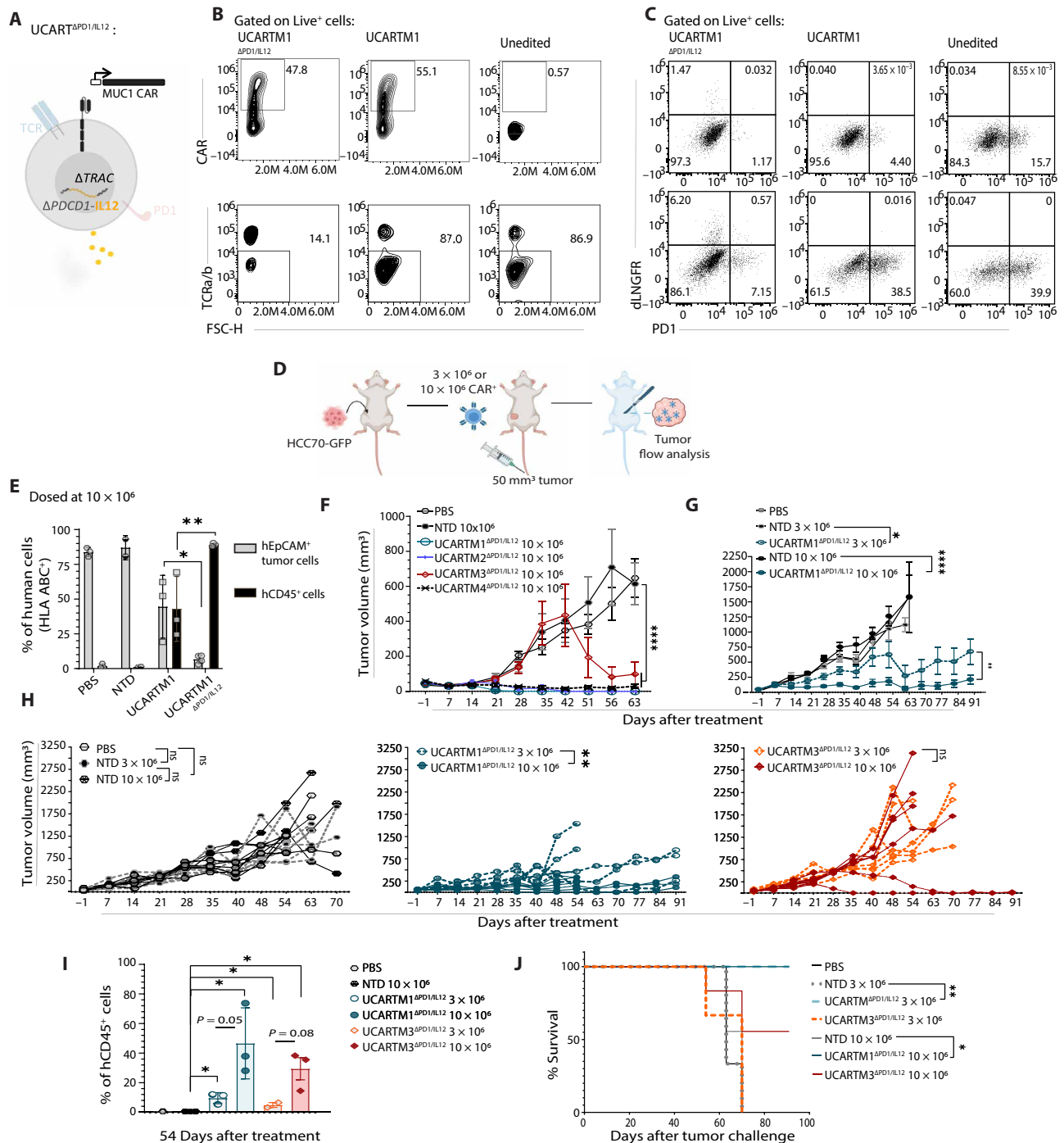
Fig. 2. PD1^{KO} and IL-12 release equipped UCARTM1 show dose-dependent tumor control, T cell infiltration, and extended survival. (**A**) Schematic representation of the non-alloreactive CAR T cell with *TRAC* and *PDCD1* knockout via TALEN, and IL-12 knock-in (UCART$^{\Delta PD1/IL12}$). Representative phenotyping of edited CAR T cells via flow cytometry analysis of (**B**) CAR expression, TCRa/b knockout, (**C**) PD1 knockout, and IL12/dLNGFR insertion detected with PMA/ionomycin activation (top panels; no PMA/ionomycin treatment; bottom panels; with PMA/ionomycin treatment). (**D**) Design of in vivo experiments. (**E**) Flow cytometry analysis of PBS-, NTD$^{\Delta PD1/IL12}$-, UCARTM1-, and UCARTM1$^{\Delta PD1/IL12}$-treated cohorts for EpCAM$^+$ and hCD45$^+$ cells among HLA-ABC$^+$ human cells engrafted, 77 days after treatment (*n* = 2 to 4 per cohort). (**F**) Tumor growth curve for cohorts treated with UCARTM1$^{\Delta PD1/IL12}$, UCARTM2$^{\Delta PD1/IL12}$, UCARTM3$^{\Delta PD1/IL12}$, UCARTM4$^{\Delta PD1/IL12}$, and NTD (*n* = 10 per cohort) or PBS (*n* = 5). (**G**) Tumor growth curve for cohorts treated with PBS (*n* = 4), different doses of NTD, and UCARTM1$^{\Delta PD1/IL12}$ (*n* = 6 per cohort). (**H**) Individual tumor growth. (**I**) Flow cytometry analysis of percent hCD45$^+$ cells in tumors. (**J**) Kaplan-Meier survival analysis of cohorts treated with either PBS (*n* = 3) or different doses of NTD, UCARTM3$^{\Delta PD1/IL12}$, and UCARTM1$^{\Delta PD1/IL12}$ (*n* = 3 to 6 per cohort). Each point represents a biological replicate for (E) to (I) and statistical significance was calculated using unpaired *t* test. Each point represents a biological replicate for (F) to (H) and mixed-effects analysis was performed for comparisons over time for tumor growth. Statistical significance was calculated using the log-rank Mantel-Cox test for the survival curve in (J). *$P < 0.05$, **$P \leq 0.01$, ****$P \leq 0.0001$, ns (not significant) indicates $P > 0.05$. Treatments were done using 3×10^6 or 10×10^6 CAR$^+$ cells as indicated on each graph.

migration and infiltration in the tumor and positively affect efficacy (*34*, *43*, *55–58*). Moreover, intratumoral administration can potentially further increase safety by localization of the CAR T cells to the tumor site rather than circulating systemically, thus limiting the risk of on-target off-tumor toxicities. To evaluate whether the M1 scFv selected for the further development of MUC1 CAR T cells displayed strong binder functions when reaching the tumor, we generated an orthotopic TNBC model carrying 50-mm^3 HCC70-GFP tumors in two contralateral mammary fat pads and treated one of the tumors intratumorally with UCARTM1 harboring no additional attributes (Fig. 3A). Using CAR T cells generated from two independent donors, we observed that while tumors in NTD and PBS cohorts grew exponentially, tumor growth was rapidly halted in tumors treated with UCARTM1 and tightly controlled throughout the course of the 80-day study (Fig. 3B and fig. S3A). In agreement, tumor weight was also significantly reduced in tumors treated with UCARTM1 compared to the NTD and contralateral PBS controls (Fig. 3C). Upon observing this significant tumor control, we dissociated and analyzed the tumors treated with UCARTM1 by flow cytometry and confirmed the presence of hCD45$^+$ cells (Fig. 3F). These results provided additional confirmation of M1 scFv binder functions in vivo without attributes while highlighting that the intratumoral method can substantially affect the efficacy of the treatment. Moreover, health and weight of animals were not affected during these studies, aside from one outlier for donor 2 (fig. S3, B and C).

In parallel, we intravenously treated another cohort carrying tumors with a similar size to the above using the same dose of UCARTM1 and compared the efficacy of intratumoral and intravenous treatments. Significant differences were observed in both tumor growth and the tumor weight with intratumoral treatment providing enhanced tumor control (Fig. 3, D and E, and fig. S3D). These results supported the importance of unarmored CAR T cell localization to increase the efficacy of UCARTM1 treatment. To validate the comparison, tumor growth in both one-tumor and two-tumor models were plotted for two donors ensuring that the average tumor growth is independent for each tumor and the two models are comparable for tumor size for controls (fig. S3E).

Intratumoral administration allows antigen recognition at distant sites while limiting CAR T cells in circulation

Patients with relapsed or refractory TNBC who can potentially benefit from CAR T cell therapy often present with metastasis, thus emphasizing the importance of antigen recognition and activity at distant sites (*59*). Therefore, we also evaluated the contralateral tumors that were treated only with PBS (as injection control) and identified cells that express hCD45 as a marker of immune cells of human origin, suggesting that intratumorally administered UCARTM1 can also migrate to distant sites. In detail, we recorded 15 hCD45$^+$ cells per 100 EpCAM$^+$ tumor cells per gram of tumor in the UCARTM1-treated tumors, and we observed an average of five hCD45$^+$ cells per 100 EpCAM$^+$ cells in the contralateral tumors treated only with PBS (Fig. 3F and fig. S3, F and G). Our findings were confirmed with IHC staining of the hCD45$^+$ cells in the treated and contralateral tumors. In contrast, we did not observe hCD45$^+$ cells in the contralateral tumors of the NTD cohort, although we detected a low number of hCD45$^+$ cells in the NTD-treated tumors (Fig. 3G). hCD45$^+$CAR T cells were 75 to 80% CD8$^+$ at both tumor sites, suggesting a similar functional potential (Fig. 3H). CAR T cells

also showed a similar differentiation profile in both tumors (fig. S3H), yet less cytotoxic activity was observed in the contralateral tumor, which could be the result of a lower effector-to-target (E:T) ratio, timing, the state of the CAR T cells reaching the distant tumor, or the immunosuppression by the TME, among others. Moreover, because UCARTM1 migrated from the initial site of injection, we additionally evaluated spleens via IHC and confirmed that they were devoid of hCD45$^+$ (Fig. 3I).

As decreased circulating CAR T cells may mitigate risks associated with off-tumor activity, we investigated CAR T cells in circulation during the study. Flow cytometry analysis of the peripheral blood collected at days 26, 40, and 80, for cohorts treated with UCARTM1, consistently revealed a minimal number of hCD45$^+$ cells ($1.1 \pm 0.1/\mu l$ for all time points) in circulation while the NTD average was 2 ± 2.3 (Fig. 3J). The percentage of hCD45$^+$cells detected in the treated cohort was also similar to the NTD controls in both donors (fig. S3I). Overall, we observed that the intratumoral administration of the UCARTM1 is superior in efficacy to intravenous administration and potentially safer without forgoing the benefits of antigen recognition at distant sites. However, it is important to emphasize that although intratumorally administered UCARTM1 harboring no additional attributes could recognize the antigen at distant sites, it could not facilitate a significant reduction at the distant tumor, thus highlighting the need for CAR T cell armoring to boost activity and overcome immunosuppression by the TME.

TGFBR2^{KO} CAR T cell editing overcomes the inhibitory effects of TGFB1 in vitro

We next sought to explore additional attributes that could help CAR T cell activity in the TME. In addition to operating as one of the key inhibitors of T cell function in the TME of solid tumors, TGFB1 pathway correlates with metastasis and poor prognosis in breast cancer (*60*, *61*). Moreover, recent evidence in pancreatic cancer links high MUC1 expression and pro-tumorigenic functions of TGFB1 (*62*). Taking this evidence into consideration, we proceeded to armor the UCARTM1 by using a TALEN to knock out *TGFBR2* (UCARTM1$^{\Delta TGFBR2}$), to prevent TGFB1-mediated T cell inhibition and potentially boost its activity in the TNBC TME (Fig. 4A). We confirmed a higher than 90% *TGFBR2* knockout efficiency by treating the UCARTM1 and UCARTM1$^{\Delta TGFBR2}$ with TGFB1 in vitro and analyzing the cells for phosphorylation of SMAD2/3, which mediates signaling downstream of the TGFBR2 pathway (*63*) (Fig. 4B). Subsequently, we validated in vitro that UCARTM1$^{\Delta TGFBR2}$ is protected against the inhibitory effects of TGFB1. For that, we measured the expression of the activation marker CD25 upon CAR T cell activation with recombinant MUC1 peptide and discovered that, in the presence of TGFB1, the percentage of cells up-regulating CD25 expression in UCARTM1 are lowered, while remaining unchanged in UCARTM1$^{\Delta TGFBR2}$ cells (Fig. 4C). We next compared the proliferation of UCARTM1 and UCARTM1$^{\Delta TGFBR2}$ in a serial re-stimulation in vitro assay in the presence or absence of TGFB1. This experiment showed significantly inhibited proliferation of UCARTM1 while expansion of UCARTM1$^{\Delta TGFBR2}$ was unaffected (Fig. 4D). Notably, while TGFBR2^{KO} did not affect activation, these cells displayed a slower proliferation profile under these conditions than UCARTM1 cells. Altogether, these in vitro experiments revealed the resistance of UCARTM1$^{\Delta TGFBR2}$ to TGFB1 while UCARTM1 activation and proliferation were significantly impaired.
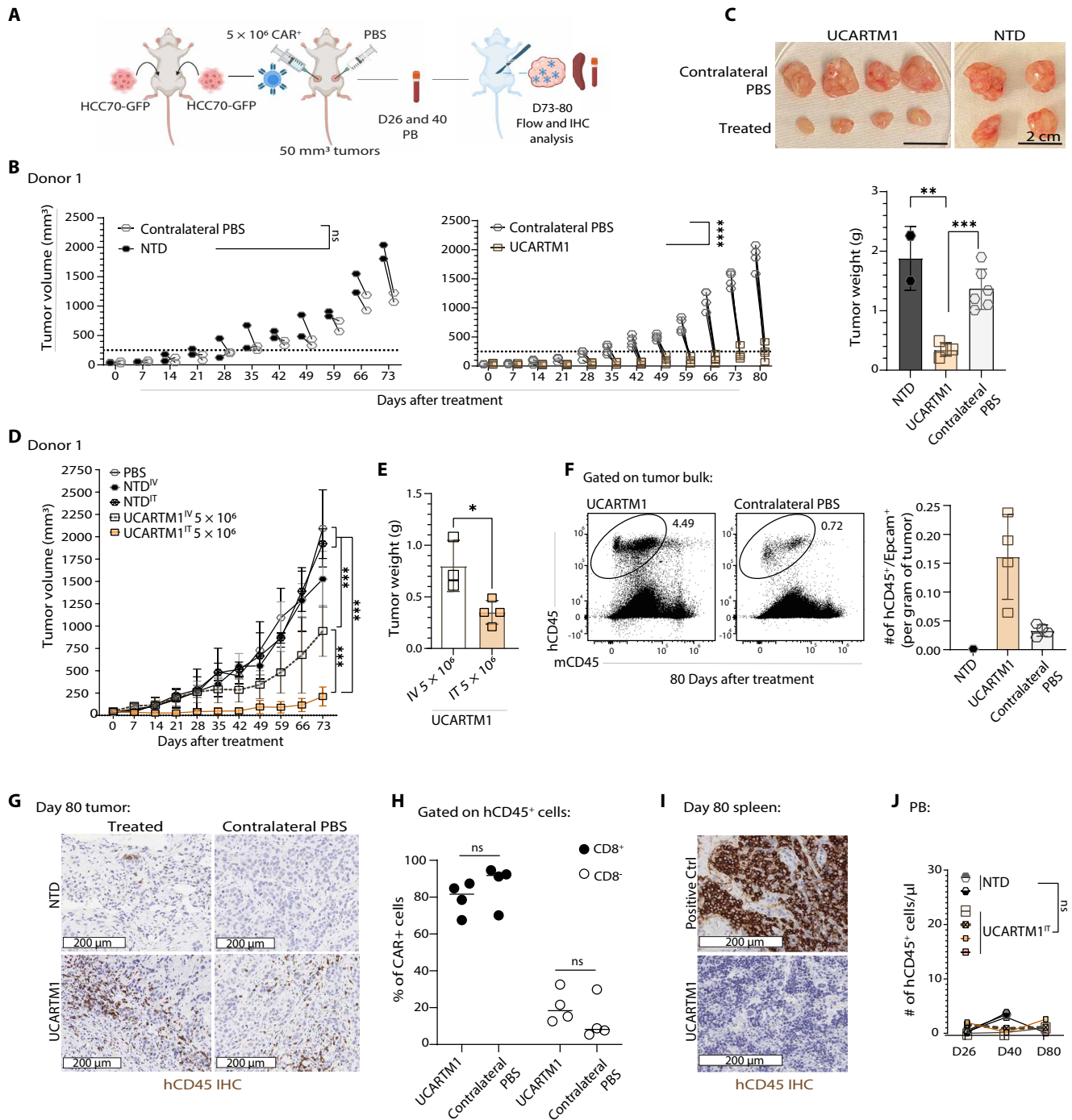
Fig. 3. Intratumoral administration of the UCARTM1 increases tumor control while still recognizing antigen at secondary site. (**A**) Design of in vivo experiment. (**B**) Tumor growth of cohorts treated intratumorally with UCARTM1 ($n = 4$) or NTD ($n = 2$) and their matched contralateral tumors that are treated with PBS (UCARTM1 engineered using donor 1). Experiment repeated with donor 2 is shown in the Supplementary Materials. (**C**) Dissection images and comparison of tumor weight for tumors treated with UCARTM1, NTD, or PBS. (**D**) Tumor growth curve comparison of tumors treated intratumorally with 5 million UCARTM1 ($n = 4$) or NTD ($n = 2$) and intravenously with 5 million UCARTM1 ($n = 5$), NTD ($n = 5$), or PBS ($n = 5$) (UCARTM1 engineered using donor 1). (**E**) Tumor weight comparison of tumors treated with 5×10^6 UCARTM1 either intratumorally or intravenously ($n = 3$ to 4). (**F**) Flow cytometry analysis of the number of hCD45$^+$ cells per EpCAM$^+$ cells per gram of tumor tumors treated with UCARTM1 and their matched contralateral PBS ($n = 4$). (**G**) Immunohistochemistry analysis of hCD45$^+$ cells in tumors in the tumors treated with UCARTM1, NTD, and their matched contralateral PBS. (**H**) Flow cytometry detection of CD8$^+$ among the hCD45$^+$CAR$^+$ cells in tumors treated with UCARTM1 and their matched contralateral PBS ($n = 4$). (**I**) Immunohistochemistry analysis of hCD45$^+$ cells spleens of the cohorts treated with UCARTM1 and staining control. (**J**) Flow cytometry analysis of PB collected from intratumorally treated UCARTM1 ($n = 4$) and NTD ($n = 2$) cohorts for days 26, 40, and 80. Each point represents a biological replicate for (B) to (J). Statistical significance was calculated using unpaired t test for (C), (E), (H), and (J). Two-way ANOVA was performed for comparisons over time for tumor growth in (D). $*P < 0.05$, $**P \leq 0.01$, $***P \leq 0.001$, $****P \leq 0.0001$, ns (not significant) indicates $P > 0.05$. All treatments were done using 5×10^6 CAR$^+$ cells.
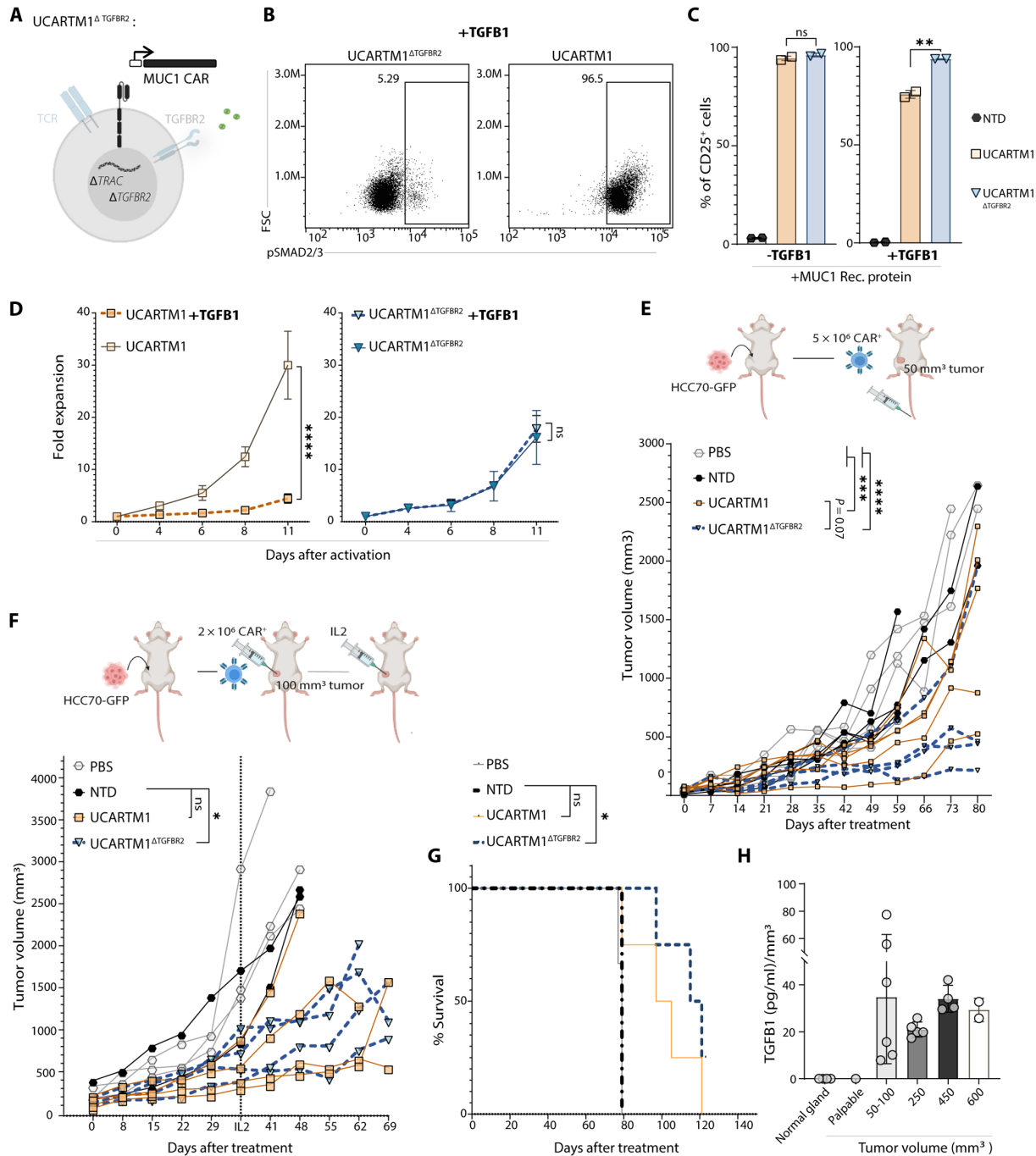
Fig. 4. TGFBR2^KO armored UCARTM1 shows resistance to inhibitory effects of TGFB1. (**A**) Schematic representation of the non-alloreactive CAR T cell with *TRAC* and *TGFBR2* knockout with TALEN (UCARTM1^ΔTGFBR2). (**B**) Functional phenotyping of *TGFBR2* knockout edited UCARTM1 compared to the unedited UCARTM1 via flow cytometry analysis of pSMAD2/3 staining in the presence of TGFB1. (**C**) Flow cytometry analysis of the percentage of CD25^+ cells present in UCARTM1 and UCARTM1^ΔTGFBR2 following activation with MUC1 recombinant protein, in the presence or absence of TGFB1 ($n = 2$). Statistical significance was calculated using unpaired *t* test. (**D**) Proliferation assay for MUC1 recombinant protein activated UCARTM1 and UCARTM1^ΔTGFBR2 in the presence or absence of TGFB1 at days 0, 4, 6, 8, and 11 ($n = 2$ technical replicates per time point). Statistical significance was determined using a two-way ANOVA. (**E**) Design of in vivo experiment and individual tumor growth comparison of tumors treated intravenously with 5 million UCARTM1^ΔTGFBR2, UCARTM1, NTD, or PBS ($n = 4$ to 5 per cohort) for donor 1. Experiment repeated with donor 2 is shown in the Supplementary Materials. Two-way ANOVA was performed for comparisons over time for tumor growth. (**F**) Design of in vivo experiment, individual tumor growth comparison of tumors, and (**G**) Kaplan-Meier survival analysis of cohorts treated intratumorally with 2 million UCARTM1^ΔTGFBR2 ($n = 4$), UCARTM1 ($n = 4$), NTD ($n = 2$), or PBS ($n = 3$). Each point represents a biological replicate for (E) to (G). Statistical significance was calculated using mixed-effects analysis comparisons over time for tumor growth and the log-rank Mantel-Cox test. *$P < 0.05$, **$P \leq 0.01$, ***$P \leq 0.001$, ****$P \leq 0.0001$, ns (not significant) indicates $P > 0.05$. (**H**) TGFB1 ELISA analysis of HCC70-GFP tumors averaging 50 to 100, 250, 450, and 600 mm^3 per mm^3 of tumor ($n = 2$ to 6). Each point represents a biological replicate. Treatments were done using 2×10^6 or 5×10^6 CAR^+ cells as indicated on each in vivo design.

UCARTM1$^{\Delta TGFBR2}$ treatment reduces heterogeneity of the tumor response and extends survival

In vitro results showed that TGFB1 did not affect activation and proliferation of UCARTM1$^{\Delta TGFBR2}$ T cells. To test the potential benefits of UCARTM1$^{\Delta TGFBR2}$ in vivo, we first confirmed the presence of TGFB1 in the TME of the orthotopic HCC70-GFP model using an enzyme-linked immunosorbent assay (ELISA) on tumor serum that detects the highly conserved TGFB1 from mouse and human origin (fig. S4A). We expected that the levels of detected cytokine originated from a combination of the tumor cells and murine TME and that both forms, human and murine, could contribute to T cell inhibition as it has been previously shown (64). Next, we intravenously treated 50-mm^3 tumors with UCARTM1 and UCARTM1$^{\Delta TGFBR2}$ and observed a decrease in average tumor growth with UCARTM1 or UCARTM1$^{\Delta TGFBR2}$ compared to the NTD and PBS controls. Tumor control of UCARTM1$^{\Delta TGFBR2}$ showed a trend toward higher efficacy but it was not significant (P value = 0.07) in this model and, therefore, the benefit of this attribute on its own in this model was not definitive. Of note, on an individual tumor basis, we observed a heterogeneous response with UCARTM1 treatment with only some tumors responding to treatment. However, with UCARTM1$^{\Delta TGFBR2}$ treatment, we observed that the heterogeneity in tumor responses was reduced (Fig. 4E and fig. S4B), while animal weight and health of the CAR T cell–treated animals were similar to control cohort (fig. S4, C and D). For instance, UCARTM1 treatment reduced the tumor size to half or less (compared to the controls, NTD and PBS) in 40% of the tumors while with UCARTM1$^{\Delta TGFBR2}$ treatment, 60 to 75% of the tumors were reduced to half the size or lower in two separate experiments using different donors. These observations suggested that there may be benefits of this attribute; however, we were unable to draw definitive conclusions in this model.

Alongside the intravenous treatment with UCARTM1$^{\Delta TGFBR2}$, we evaluated the efficacy of UCARTM1$^{\Delta TGFBR2}$ in the contralateral tumor model using intratumoral treatment (fig. S4F). Similar to UCARTM1, we observed both specific recognition of the antigen at a distant site by hCD45$^+$CD8$^+$ CAR T cells (fig. S4, G to J) and enhanced tumor control of intratumorally treated UCARTM1$^{\Delta TGFBR2}$ compared to the intravenously treated UCARTM1$^{\Delta TGFBR2}$ (both at a dose of 5 million CAR T cells), NTD, and PBS controls, with no effect on animal weight and health (fig. S4, K to N). In the UCARTM1$^{\Delta TGFBR2}$-treated cohort, we also noted an increase in the number of hCD45$^+$ cells in circulation for 50% of the animals on day 26 (18 ± 0.4/μl), which decreased at day 80 (0.75 ± 0.2/μl) in comparison to the steadily low levels of UCARTM1 (fig. S4O). Overall, average circulating cells remained lower than the injection dose of the intravenous treatment.

Observing similar efficacies for both UCARTM1 and UCARTM1$^{\Delta TGFBR2}$ upon intratumoral treatment with 5 million CAR T cells (fig. S4M), we compared the two CAR T cells at a decreased dose and doubled tumor volume. This allowed us to evaluate a more stringent E:T ratio and further interrogate potential advantages of TGFBR2^{KO}. For that, we intratumorally treated 100-mm^3 tumors with 2 million UCARTM1 or UCARTM1$^{\Delta TGFBR2}$, which resulted in a reduced tumor control compared to the previously used dose of 5 million CAR T cells as expected. As the average tumor volume approached 1000 mm^3 for the CAR T cell–treated cohorts and no significant tumor control was observed, we injected IL-2 to support T cell proliferation. In this model, we observed a slight increase in survival for UCARTM1$^{\Delta TGFBR2}$ treatment but that was not significantly

higher than UCARTMUC1 (Fig. 4, F and G). In addition, animal weight and health were comparable to the controls throughout the experiment (fig. S4E).

To explore how TGFBR2^{KO} could reduce the heterogeneity in the tumor responses obtained, we performed a TGFB1 ELISA on the serum of varying sizes of tumors. We discovered that at 50–100 mm^3, tumors show great variability of TGFB1 in the TME per cubic millimeter of tumor, potentially explaining the heterogeneity of responses seen with UCARTM1 treatment without the protective effects of TGFBR2^{KO} (Fig. 4H). We also identified that at 450 mm^3, HCC70-GFP tumors provide the highest and most consistent TGFB1 levels per cubic millimeter. Thus, a cohort was set up to compare UCARTM1$^{\Delta TGFBR2}$ with UCARTM1 activity in 450-mm^3 tumors using two doses of 5 million CAR$^+$ T cells administered intratumorally for two consecutive weeks but was unable to robustly control the high tumor burden (fig. S4, P and Q). This observation highlighted the need for further attributes to boost cell proliferation and function in vivo while providing resistance to inhibitory mechanism of the TME.

PD1^{KO}, IL-12^{KI}, and TGFBR2^{KO} edited UCARTM1 clear tumors without relapse and accelerate the reduction of immune cells at the tumor site

Our results above showed that, to mount an efficient CAR T cell response in the hostile solid tumor TME, armoring the CAR T cells confers an advantage and that each attribute provides specific benefits. Therefore, we next sought to combine the attributes and evaluate the multi-armored MUC1 CAR T cells for potential benefits. We engineered UCARTM1$^{\Delta PD1/IL12;\ \Delta TGFBR2}$ that show a high level of engineering with a CAR expression ~50% in all cases and >80% $TRAC^{KO}$ that was increased to close to 100% upon enrichment to prevent graft-versus-host disease (fig. S5A). The rest of the edits were measured at the genomic level by locus-specific polymerase chain reaction (PCR) coupled with next-generation sequencing for $PDCD1$ and $TGFBR2$ and ddPCR for IL-12, as the identification of these edits via flow cytometry requires activation of the cells or treatment with TGFB1, leading to less accurate results. As the TALEN editing efficiency is similar in CAR-positive and -negative cells, we expected that the total editing efficiencies in the CAR-expressing T cells were similar to the editing efficiency observed in the bulk cells (fig. S5, A and B). We first confirmed that these CAR T cells overcome TGFB1-mediated inhibition while TGFB1 significantly impairs expansion of UCARTM1$^{\Delta PD1/IL12}$ in vitro in the presence of MUC1 recombinant protein (Fig. 5B). Moreover, we performed an in vitro cytotoxic assay in the presence of TGFB1 and detected higher tumor killing activity by UCARTM1$^{\Delta PD1/IL12;\ \Delta TGFBR2}$ against the T47D-GFP tumor cell challenge and the re-challenge in comparison to UCARTM1$^{\Delta PD1/IL12}$, UCARTM1$^{\Delta TGFBR2}$, UCARTM1, and NTD (Fig. 5C). Next, to investigate the tumor-killing efficacy of the CAR T cells carrying multiple attributes, we treated tumors intravenously with UCARTM1, UCARTM1$^{\Delta TGFBR2}$, UCARTM1$^{\Delta PD1/IL12}$, UCARTM1$^{\Delta PD1/IL12;\ \Delta TGFBR2}$, NTD, and PBS controls at 50 mm^3 with a 5 million CAR$^+$ dose (Fig. 5D). While tumors in the control groups NTD and PBS grew exponentially, and UCARTM1 and UCARTM1$^{\Delta TGFBR2}$ treatments resulted in some reduction of the tumor, UCARTM1$^{\Delta PD1/IL12}$- or UCARTM1$^{\Delta PD1/IL12;\ \Delta TGFBR2}$-treated tumors were cleared in 2 to 3 weeks after treatment (Fig. 5E and fig. S5C). Flow cytometry analysis performed on PB, on days 26 and 40, revealed a significantly higher percentage of hCD45$^+$ cells in circulation for
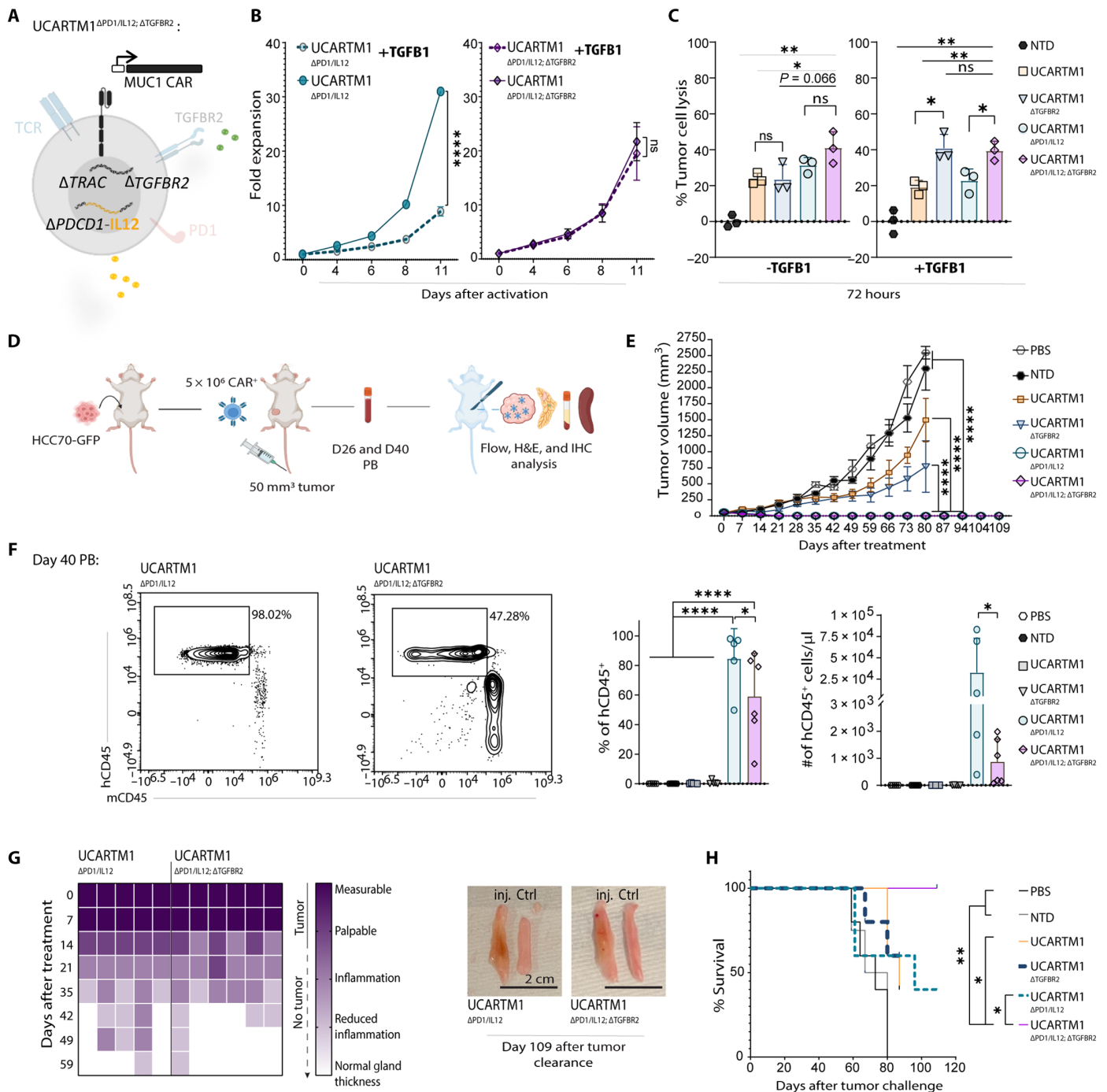
Fig. 5. PD1^KO/IL-12^KI and TGFBR2^KO armored CAR T cells clear tumors within weeks without relapse with less CAR T cell expansion. (**A**) Schematic representation of the non-alloreactive CAR T cell with *TRAC*, *PDCD1*, and *TGFBR2* knockouts and IL-12 knock-in. (**B**) Proliferation assay of MUC1 recombinant protein–activated UCARTM1$^{\Delta PD1/IL12}$ and UCARTM1$^{\Delta PD1/IL12; \Delta TGFBR2}$ with or without TGFB1 ($n = 2$ technical replicates per time point). Two-way ANOVA was performed for statistical significance over time. (**C**) Cytotoxic assay of T47D cells cocultured with NTD, UCARTM1, UCARTM1$^{\Delta TGFBR2}$, UCARTM1$^{\Delta PD1/IL12}$, and UCARTM1$^{\Delta PD1/IL12; \Delta TGFBR2}$ in the presence of TGFB1 with a 10-to-1 E:T ratio. CAR T cells were rechallenged after 24 hours ($n = 3$). Each point represents a technical replicate. Statistical significance was calculated using unpaired *t* test. (**D**) Design of in vivo experiment. (**E**) Tumor growth curve for cohorts intravenously treated with 5 million UCARTM1$^{\Delta PD1/IL12; \Delta TGFBR2}$, UCARTM1$^{\Delta PD1/IL12}$, UCARTM1$^{\Delta TGFBR2}$, UCARTM1, NTD, or PBS ($n = 5$ to 6 per cohort) and (**F**) flow cytometry analysis of PB collected from all cohorts, 40 days after treatment for number and percent of hCD45$^+$ cells. Two-way ANOVA was performed for comparisons for tumor growth, and ordinary one-way ANOVA was performed to determine the statistical significance for (F). (**G**) Color mapping of tumor clearance and inflammation in the mammary glands of UCARTM1$^{\Delta PD1/IL12}$- and UCARTM1$^{\Delta PD1/IL12; \Delta TGFBR2}$-treated cohorts ($n = 5$ and 6, consecutively) and representative dissection images of tumor cell injected (inj.) and no tumor cell injected mammary fat pad (MFP) (Control; Ctrl) of one animal each. (**H**) Kaplan-Meier survival analysis of cohorts treated with UCARTM1$^{\Delta PD1/IL12; \Delta TGFBR2}$, UCARTM1$^{\Delta PD1/IL12}$, UCARTM1$^{\Delta TGFBR2}$, UCARTM1, NTD, or PBS ($n = 4$ to 6 per cohort). Each point represents a biological replicate for (E) to (G). Statistical significance was calculated using the log-rank Mantel-Cox test in (H). *$P < 0.05$, **$P \leq 0.01$, ****$P \leq 0.000$, ns (not significant) indicates $P > 0.05$. All treatments were done using 5×10^6 CAR$^+$ cells.

both UCARTM1$^{\Delta PD1/IL12}$- and UCARTM1$^{\Delta PD1/IL12;\,\Delta TGFBR2}$-treated cohorts compared to other cohorts (Fig. 5F and fig. S5D). Although the tumor clearance was comparable with both UCARTM1$^{\Delta PD1/IL12}$ and UCARTM1$^{\Delta PD1/IL12;\,\Delta TGFBR2}$ treatments, at day 40 PB analysis, UCARTM1$^{\Delta PD1/IL12;\,\Delta TGFBR2}$-treated cohorts showed a significantly lower number and percentage of hCD45$^+$ cells while circulating levels of UCARTM1$^{\Delta PD1/IL12}$ remained high.

Mammary fat pads were also monitored each week after tumor clearance and compared in thickness to the non–tumor-injected, normal contralateral mammary fat pads by palpation. The mammary glands of the UCARTM1$^{\Delta PD1/IL12;\,\Delta TGFBR2}$-treated cohort qualitatively showed an accelerated recovery to the normal thickness of the gland (Fig. 5G). This observation was further investigated with hematoxylin and eosin (H&E) and trichrome staining of the glands at study termination, revealing that the thickness of the gland was correlated to immune cell presence and not to scarring/collagen deposition or remaining tumor cells (fig. S5, E and F). In addition, we confirmed that there were no residual tumor cells in the mammary glands in this H&E analysis. Both UCARTM1$^{\Delta PD1/IL12;\,\Delta TGFBR2}$ and UCARTM1$^{\Delta PD1/IL12}$ T cell–treated cohorts were monitored for 109 days and did not show tumor relapse (Fig. 5E). Spleen IHC analysis of both cohorts confirmed the presence of hCD45$^+$ cells, yet a lower number of hCD45$^+$ cells was observed in the UCARTM1$^{\Delta PD1/IL12;\,\Delta TGFBR2}$-treated cohort (fig. S5G). Moreover, the UCARTM1$^{\Delta PD1/IL12;\,\Delta TGFBR2}$-treated cohort showed significantly extended survival over all cohorts including the UCARTM1$^{\Delta PD1/IL12}$-treated cohort, and animal health and weight were similar to those of the NTD- and PBS-treated controls (Fig. 5H and fig. S5H). Overall, we observed high efficacy of the tumor killing for both UCARTM1$^{\Delta PD1/IL12}$ and UCARTM1$^{\Delta PD1/IL12;\,\Delta TGFBR2}$ in this model. However, our results showing that UCARTM1$^{\Delta PD1/IL12;\,\Delta TGFBR2}$ presents with a lower number of CAR T cells in PB at day 40 and spleen at day 109 after treatment, a faster reduction of immune response after tumor clearance of the mammary fat pad, and a survival advantage support the hypothesis that TGFBR2^{KO} confers additional benefits synergistically with PD1^{KO} and IL-12^{KI} attributes.

Intratumorally administered UCARTM1$^{\Delta PD1/IL12;\,\Delta TGFBR2}$ kill contralateral tumors in a high–tumor burden model with lower systemic distribution of CAR T cells

We demonstrated above that intratumoral administration can limit CAR T cells in circulation while allowing antigen recognition at distant sites. We next sought to evaluate both local and distant efficacy and the potential benefits of intratumorally administered UCARTM1$^{\Delta PD1/IL12;\,\Delta TGFBR2}$ in a high–tumor burden model with high levels of TGFB1. Because intratumoral treatment was more efficient than intravenous treatment, we hypothesized that a reduced dose of UCARTM1 with multiple attributes should display good activity and, therefore, we proceeded to lower the treatment to 1 million UCARTM1$^{\Delta PD1/IL12;\,\Delta TGFBR2}$ and increase the total tumor burden to 900 mm^3. We established two TGFB1-rich tumors at 450 mm^3 in each mammary fat pad and intratumorally treated only one of the tumors with either UCARTM1$^{\Delta PD1/IL12}$ or UCARTM1$^{\Delta PD1/IL12;\,\Delta TGFBR2}$ along with a cohort for UCARTM1 harboring no attributes and NTD control (Fig. 6A). As previously described, we injected PBS in the contralateral tumors of all cohorts as injection control. UCARTM1- and NTD-treated tumors and their contralateral PBS tumors grew exponentially, while UCARTM1$^{\Delta PD1/IL12;\,\Delta TGFBR2}$ treatment showed a remarkable reduction in tumor volume for both the treated and the

contralateral tumor sites starting 2 weeks after treatment (Fig. 6B and fig. S6A). In contrast, the UCARTM1$^{\Delta PD1/IL12}$ treatment produced more variable responses, where treatment was effective at the 2-week time point in some animals while others did not respond or showed a delayed reduction in tumor volume. In the UCARTM1$^{\Delta PD1/IL12;\,\Delta TGFBR2}$-treated cohort, tumor killing was accelerated in the treated tumors in comparison to UCARTM1$^{\Delta PD1/IL12}$, UCARTM1, and NTD, as we recorded significant reduction of both tumor weight and number of EpCAM$^+$ cells at day 22 after treatment (Fig. 6, C and D). Flow cytometry analysis of the treated and contralateral tumors at this time point showed a similar number of hCD45$^+$ and EpCAM$^+$ cell ratio per gram of tumor for UCARTM1$^{\Delta PD1/IL12}$- and UCARTM1$^{\Delta PD1/IL12;\,\Delta TGFBR2}$-treated cohorts, suggesting the increased efficacy of CAR T cell activity upon combination of attributes (Fig. 6E and fig. S6B). Moreover 5 weeks after treatment, both treated and contralateral tumors of the UCARTM1$^{\Delta PD1/IL12;\,\Delta TGFBR2}$ treatment cohort were completely reduced to tumor sizes that were not palpable, while in the UCARTM1$^{\Delta PD1/IL12}$-treated cohort, there were measurable tumors remaining (Fig. 6B). For the responders remaining at day 49, the mammary glands (with and without palpable tumors) were excised whole for both cohorts, and we noted significantly lower weight for the UCARTM1$^{\Delta PD1/IL12;\,\Delta TGFBR2}$ treated group and the contralateral mammary fat pads after tumor clearance or reduction in comparison to UCARTM1$^{\Delta PD1/IL12}$ and the NTD treatment (fig. S6C). We further confirmed that the weight difference is due to the larger tumor mass and the abundance of immune infiltration remaining in the UCARTM1$^{\Delta PD1/IL12}$-treated cohort in comparison to the UCARTM1$^{\Delta PD1/IL12;\,\Delta TGFBR2}$, with an IHC staining for hCD8$^+$ CAR T cells and GFP$^+$ tumor cells, and an H&E analysis, once again suggesting increased efficacy of the UCARTM1 with combined attributes (Fig. 6F and fig. S6, D and E). Overall, both UCARTM1$^{\Delta PD1/IL12}$- and UCARTM1$^{\Delta PD1/IL12;\,\Delta TGFBR2}$-treated cohorts showed extended survival compared to the NTD controls; however, because of the remarkable tumor reduction achieved in the UCARTM1$^{\Delta PD1/IL12;\,\Delta TGFBR2}$-treated cohort, survival was extended over the UCARTM1$^{\Delta PD1/IL12}$-treated cohort (Fig. 6G). Animal weight and health of the CAR T cell–treated animals were similar to the control cohort, although few animals in the UCARTM1$^{\Delta PD1/IL12}$-treated cohort showed reduction in body weight 3 weeks after treatment but a consecutive recovery (fig. S6F).

In parallel, we performed flow cytometry analysis on PB collected at day 26, to investigate the number of CAR T cells in circulation as tumors on both mammary fat pads were getting reduced simultaneously. Notably, although the contralateral tumors were more effectively controlled upon UCARTM1$^{\Delta PD1/IL12;\,\Delta TGFBR2}$ treatment compared to UCARTM1$^{\Delta PD1/IL12}$, the percentage and number of hCD45$^+$ cells in PB of UCARTM1$^{\Delta PD1/IL12;\,\Delta TGFBR2}$ were significantly lower (Fig. 7A). Moreover, in the low number of hCD45$^+$ cells detected in circulation, the percentage of CD8$^+$ cells were significantly higher for UCARTM1$^{\Delta PD1/IL12;\,\Delta TGFBR2}$ T cell treatment compared to the UCARTM1$^{\Delta PD1/IL12}$ cells, which may suggest a potentially higher cytotoxic capacity for this population of CAR T cells (Fig. 7A). In addition, we observed that while there was a significant increase in the spleen size of the UCARTM1$^{\Delta PD1/IL12}$-treated cohort, spleens in the UCARTM1$^{\Delta PD1/IL12;\,\Delta TGFBR2}$-treated cohort remained comparable to the NTD control (Fig. 7B). Elaborating on this observation, we analyzed spleens at days 22 and 49 after treatment with flow cytometry and, consistent with the differences observed in spleen sizes, we recorded a lower number of hCD45$^+$ cells in the UCARTM1$^{\Delta PD1/IL12;\,\Delta TGFBR2}$-treated cohort in comparison
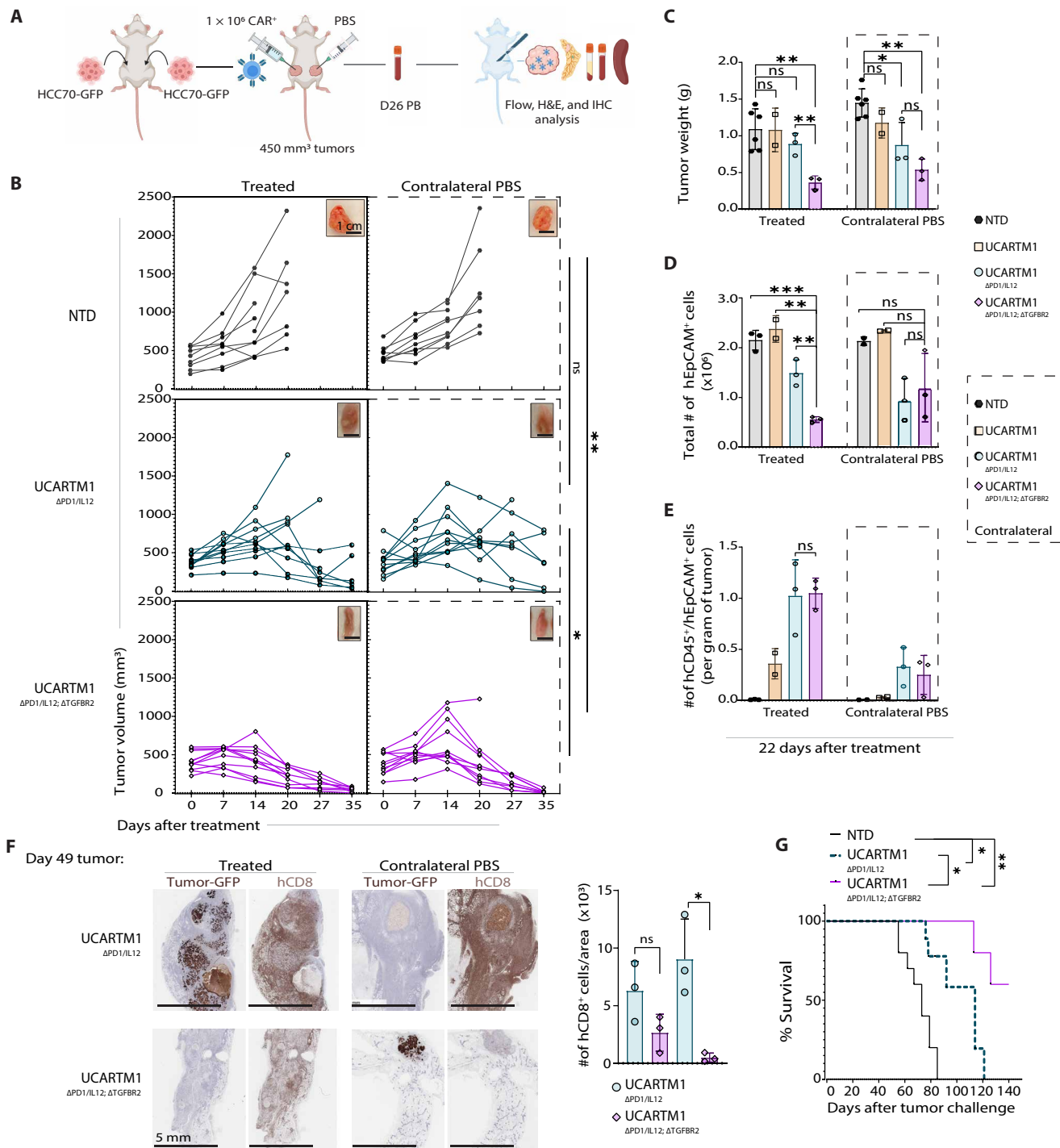
Fig. 6. Intratumoral administration of UCARTM1$^{\Delta PD1/IL12; \Delta TGFBR2}$ remarkably reduces large tumors even at distant sites and extends survival. (A) Design of in vivo experiment. (**B**) Tumor growth curve ($n = 9$ to 11, pooled from two experiments using the same donor) and representative tumor images at termination; (**C**) tumor weight comparison of cohorts intratumorally treated with 1 million UCARTM1$^{\Delta PD1/IL12; \Delta TGFBR2}$, UCARTM1$^{\Delta PD1/IL12}$, or NTD and their matched contralateral PBS tumors ($n = 2$ to 6). Each point represents a biological replicate. Statistical significance was calculated using mixed-effects analysis comparisons over time for tumor growth. Flow cytometry analysis of tumors (**D**) for total number of EpCAM$^+$ cells and (**E**) the number of hCD45$^+$ cells per EpCAM$^+$ cells found per gram of tumor in UCARTM1$^{\Delta PD1/IL12; \Delta TGFBR2}$-, UCARTM1$^{\Delta PD1/IL12}$-, UCARTM1-, or NTD-treated cohorts and their matched contralateral PBS tumors ($n = 2$ to 3). (**F**) Immunohistochemistry analysis of hCD8$^+$ and GFP$^+$ tumor cells in UCARTM1$^{\Delta PD1/IL12; \Delta TGFBR2}$ or UCARTM1$^{\Delta PD1/IL12}$ and their matched contralateral PBS tumors on day 49 after treatment ($n = 3$). Each point represents a biological replicate for (D) to (F). Statistical significance was calculated using unpaired t test for (D) and (E). (**G**) Kaplan-Meier survival analysis of cohorts treated with 1 million UCARTM1$^{\Delta PD1/IL12; \Delta TGFBR2}$, UCARTM1$^{\Delta PD1/IL12}$, or NTD ($n = 5$ to 10 per cohort, pooled from two experiments using the same donor). Statistical significance was calculated using the log-rank Mantel-Cox test for (G). *$P < 0.05$, **$P \leq 0.01$, ***$P \leq 0.001$, ns (not significant) indicates $P > 0.05$. All treatments were done using 1×10^6 CAR$^+$ cells.
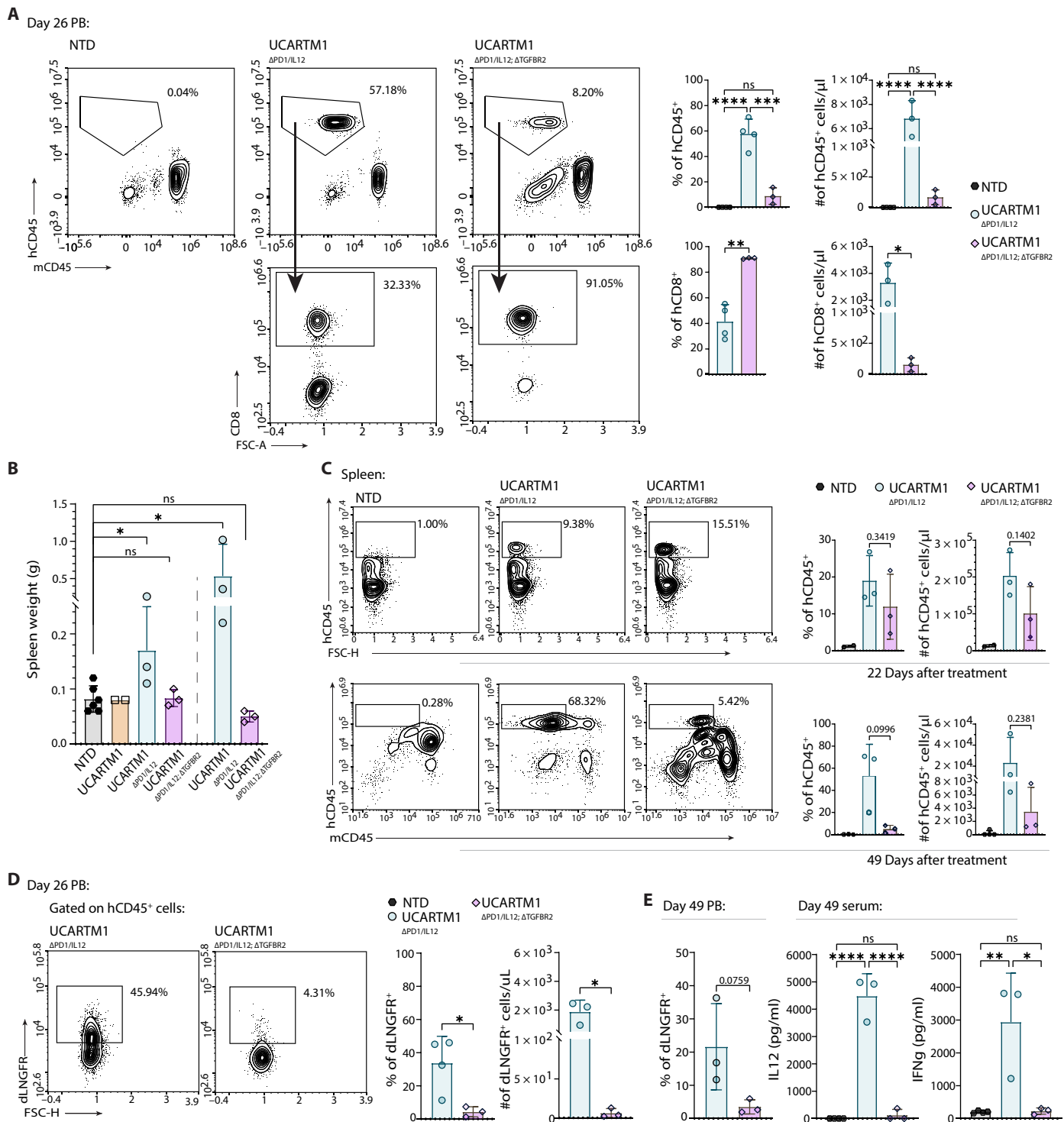
Fig. 7. Synergy of the attributes limit off tumor CAR T cells and IL-12. (**A**) Flow cytometry analysis of PB, 26 days after treatment for the percent and the number of hCD45$^+$ and hCD45$^+$CD8$^+$ cells per microliter of PB for NTD-, UCARTM1$^{\Delta PD1/IL12}$-, or UCARTM1$^{\Delta PD1/IL12; \Delta TGFBR2}$-treated cohorts ($n = 3$ to 4). (**B**) Spleen weight comparison of NTD-, UCARTM1$^{\Delta PD1/IL12}$-, or UCARTM1$^{\Delta PD1/IL12; \Delta TGFBR2}$-treated cohorts ($n = 2$ to 6). (**C**) Flow cytometry analysis of spleens for the percent and the number of hCD45$^+$ cells in cohorts treated with NTD, UCARTM1$^{\Delta PD1/IL12}$, or UCARTM1$^{\Delta PD1/IL12; \Delta TGFBR2}$ ($n = 2$ to 3). (**D**) Flow cytometry analysis of PB for UCARTM1$^{\Delta PD1/IL12; \Delta TGFBR2}$-, UCARTM1$^{\Delta PD1/IL12}$-, or NTD-treated cohorts for percent and number of hCD45$^+$dLNGFR$^+$ cells ($n = 3$ to 4). (**E**) Flow cytometry analysis of hCD45$^+$ for % of dLNGFR$^+$ cells on day 49 in PB and the corresponding IL-12 and IFN G ELISA analysis of blood serum collected from UCARTM1$^{\Delta PD1/IL12}$- and UCARTM1$^{\Delta PD1/IL12; \Delta TGFBR2}$-treated cohorts at 49 days after treatment ($n = 3$ to 4). NTD blood serum shown is collected on day 26 (controls reached termination). Each point represents a biological replicate for (A) to (E). Statistical significance was calculated using unpaired t test or ordinary one-way ANOVA. *$P < 0.05$, **$P \leq 0.01$, ***$P \leq 0.001$, ****$P \leq 0.0001$, ns (not significant) indicates $P > 0.05$.

to the UCARTM1$^{\Delta PD1/IL12}$-treated cohort's spleens (Fig. 7C and fig. S7A). Both PB and spleen analysis results highlighted the low number of cells in circulation following UCARTM1$^{\Delta PD1/IL12;\ \Delta TGFBR2}$ treatment while showing increased efficacy in tumor killing.

TGFBR2^{KO} attribute increases safety of UCARTM1 by lowering IL-12 release in synergy with PD1^{KO}/IL-12^{KI}

As high systemic levels of IL-12 can contribute to potential toxicities, as a surrogate marker for the IL-12 knock-in, we monitored surface expression of dLNGFR in both of our intravenous and intratumoral models treated with UCARTM1$^{\Delta PD1/IL12}$ and UCARTM1$^{\Delta PD1/IL12;\ \Delta TGFBR2}$. An observation we made during our PB analysis, for both the intravenous and the intratumoral models, was the enrichment of dLNGFR$^+$ cells in the PB of the UCARTM1$^{\Delta PD1/IL12}$-treated cohort while the percentage and number of hCD45$^+$dLNGFR$^+$ cells remained low in the UCARTM1$^{\Delta PD1/IL12;\ \Delta TGFBR2}$-treated cohort, despite the two CAR T cells exhibiting similar initial percent IL12-dLNGFR knock-in (Fig. 7D and figs. S5A and S7, C and D). To investigate the potential downstream effects of this enrichment, for the responders remaining at day 49, we measured the % of hCD45$^+$dLNGFR$^+$ cells in peripheral blood and used the blood serum of the same samples to perform an ELISA to analyze for IL-12 and interferon-gamma (IFNG), a marker of T cell cytotoxicity that can be expressed upon IL-12 signaling. For the intratumoral model, in agreement with the low hCD45$^+$dLNGFR$^+$ cells detected in the PB, we detected a very low amount of IL-12 and IFNG in the UCARTM1$^{\Delta PD1/IL12;\ \Delta TGFBR2}$-treated cohort comparable to the levels in NTD controls, and these levels were also significantly lower compared to the UCARTM1$^{\Delta PD1/IL-12}$-treated cohort (Fig. 7E). As expected, a significant correlation was observed between IL-12 and IFNG serum levels throughout the experimental cohorts (fig. S7E). In agreement with the intratumoral model, we also detected increased IL-12 serum levels in the intravenous model shown in Fig. 5D, for the UCARTM1$^{\Delta PD1/IL12}$ cohort, while the UCARTM1$^{\Delta PD1/IL12;\ \Delta TGFBR2}$-treated cohort showed similar levels to PBS- and NTD-treated cohorts (fig. S7F).

Further investigation of the tumors dissected at day 22 in the intratumorally treated high–tumor burden model similarly revealed a trend of hCD45$^+$dLNGFR$^+$ cell enrichment in the UCARTM1$^{\Delta PD1/IL-12}$-treated tumors compared to the UCARTM1$^{\Delta PD1/IL12;\ \Delta TGFBR2}$-treated ones (fig. S7G), suggesting that the enrichment may be initiated at the tumor site potentially due to a mechanism related to TGFB1 in the TME. Altogether, these results suggest that UCARTM1$^{\Delta PD1/IL12;\ \Delta TGFBR2}$ can be effective against a high tumor burden with high TGFB1 levels at multiple tumor sites, while limiting the number of CAR T cells and IL-12 in circulation, thus reducing the potential risks of both off-tumor and IL-12–related systemic toxicities.

DISCUSSION

Solid tumors such as TNBC present many challenges that impair CAR T cell function and limit its therapeutic success. Overcoming the complexity of solid tumors may require multifaceted strategies such as armoring CAR T cells and implementing alternative delivery routes to increase efficacy while maintaining safety. All these strategies initially build on selection of a tumor-specific antigen and viability of the cells. Ongoing investigation on autologous CAR T cell therapies targeting MUC1, in both clinical and preclinical settings, supports the therapeutic potential of this target for further clinical development (65–68). However, limitations to autologous CAR T cell therapies, such as the manufacturing time while the health of late-stage patients rapidly deteriorate, or the unreliable vigor of the acquired patient T cells at late stages of disease, highlight the importance of readily available healthy donor–derived CAR T cells (69). This is especially important in cases when advanced CAR T cell engineering is required, such as for solid tumors. We aimed to address this therapeutic need by first selecting an scFv that showed good binding to a wide range of breast tumors from different malignancy stages, while suggesting selective binding to tumor-specific MUC1 antigen. Because it has been demonstrated that cancer cells have hypoglycosylated MUC1 that is recognized specifically (70), we did not focus on this aspect experimentally, yet it would be worthwhile to further explore the on-target/off-target profile of our chosen scFv for future clinical development.

As previously shown, MUC1 CAR T cells including only the CAR was not sufficient to exert robust tumor control in vivo against HCC70-derived TNBC tumors, and PD-L1/PD1 signaling contributed to this inefficacy (71). Therefore, our main goal was to multi-armor the CAR T cells and confer a combination of advantages to enhance their function in overcoming solid tumor challenges. Our molecular armoring of UCARTM1 with PD1^{KO} and inducible IL-12 attributes enhanced both the proliferation and infiltration of the TNBC tumors expressing PD-L1, significantly reducing tumors in a dose-dependent manner and extending survival.

Our next armoring strategy aimed to equip the UCARM1 against further immunosuppression by the TME. Our in vitro findings supported the idea that TGFBR2^{KO} allows UCARTM1 to resist TGFB1-mediated inhibition of activation and proliferation. While the cytotoxic capacity and activation as measured by CD25 expression levels were not impaired in TGFBR2^{KO} CAR T cells, the ability of these cells to proliferate in vitro appeared to be decreased under these experimental conditions. While a study by Tang et al. (64) evaluating and studying knockout of TGFBR2 in CAR T cells has not shown this effect, other pieces of literature have shown differences in proliferation elicited by TGFBR2^{KO}. In various studies, TGFBR2 has been described to positively and negatively affect cell proliferation in different cell types and contexts (72–74). However, to our knowledge, no molecular mechanism has been described and further studies are warranted to shed light on this aspect.

In the intravenous treatment of tumors with UCARTM1$^{\Delta TGFBR2}$, we observed a tendency to display a more uniform response to treatment that could be related to the varying levels of TGFB1 in the TME, and in the intratumoral model, we observed increased hCD45$^+$ cells in the peripheral blood compared to TGFBR2^{WT} UCARTM1. Similarly, in a clinical trial assessing PSMA-CAR T cells with dominant negative TGFBR2 expression, a better expansion in patient blood and better control of the tumors were shown in their preclinical models (75). However, TGFBR2^{KO} attribute alone was less efficient to control larger tumors, which is a more clinically relevant tumor burden for advanced-stage tumors with high TGFB1 levels. Thus, our data suggested the need for a synergistic attribute to increase the efficacy for higher tumor burden and to better decipher the potential advantages associated with TGFBR2^{KO} attribute.

Furthermore, we sought to preclinically evaluate the benefits of intratumoral administration of the CAR T cell therapy for TNBC, measuring the efficacy of the treatment at the treated and distant tumors while monitoring the effect on the number of CAR T cells in circulation. We observed a significant tumor reduction when we

treated TNBC tumors intratumorally with UCARTM1$^{\Delta TGFBR2}$ and UCARTM1 compared to intravenous treatment, suggesting that intratumoral treatment can work at lower doses with higher efficacy for solid tumors. Similar to our observations, in a study investigating the efficacy of autologous MESO CAR T cells with TGFBR2^{KO}, targeting PDX models pancreatic carcinoma, a more effective and uniform control was also shown when CAR T cells were delivered intratumorally (64). Our data consistently showed that CAR T cells were detected in circulation and at distant tumor sites following intratumoral administration of UCARTM1. In support of our observation, in a previous clinical trial in two of six patients with metastatic breast cancer, CAR T cells were detected in circulation after c-Met-CAR T cells were delivered intratumorally (43). Thus, intratumoral injection of breast tumors can be a viable delivery option for metastatic disease. Moreover, we observed fewer cells in circulation for the intratumoral UCARTM1 with or without attributes compared to the intravenous route. These findings support the idea that intratumoral injection allows us to reduce the systemic distribution of CAR T cells significantly compared to intravenous treatment, adding another tier of safety to reduce off-tumor toxicity while preserving the potential to recognize metastasis.

Combining different attributes and alternative routes of delivery, we next discovered a synergy between PD1^{KO}/IL-12^{KI} and TGFBR2^{KO} attributes in increasing the efficacy and safety of the CAR T cell therapy. With UCARTM1$^{\Delta PD1/IL12;\ \Delta TGFBR2}$ treatment, a similar tumor reduction was possible with a lower number of CAR T cell expansion and infiltration in both intravenous and intratumoral models compared to the TGFBR2^{WT} control. In line with our findings, there is recent evidence of a therapeutic synergy between TGFB1 blockade/knockout and PD1 blockade/knockout (64, 76). We did not detect an increase in IL-12 or IFNG in the serum of UCARTM1$^{\Delta PD1/IL12;\ \Delta TGFBR2}$-treated animals and observed homing of fewer T cells to the spleen during active tumor killing and after tumor clearance. These findings suggest an additional interaction between these pathways enhancing the safety of the CAR T cell that, to our knowledge, has not yet been reported. In other studies, PD1 up-regulation was noted in the presence of TGFB1 (64, 77), suggesting that when TGFBR2 receptor is disabled, PD1 locus will not be transcriptionally activated through the indirect effects of the TGFB1 pathway. A similar interaction between the attributes may yield less IL-12 release in the UCARTM1$^{\Delta PD1/IL12;\ \Delta TGFBR2}$ while the CAR T cells reduce the tumors with increased efficacy due to resistance to both PD-L1 and TGFB1 inhibitory effects.

Moreover, previous studies highlight the importance of the TGFB1 pathway and demonstrate that in breast cancer, metastatic sites are enriched in TGFB1 (78). Here, by determining the highest levels of TGFB1 at 450-mm^3 tumors and challenging the UCARTM1$^{\Delta PD1/IL12;\ \Delta TGFBR2}$ with TGFB1-rich local and distant TNBC tumors that express PD-L1, we highlighted the effectiveness of the armored UCARTM1 antitumor activity against the immunosuppressive TME. However, a limitation of this study was that a metastatic mouse model targeting organs that TNBC commonly metastasizes to was not assessed yet given the robust responses we observed with our model, and we expect similar antigen recognition. Further clinical studies are needed to investigate the feasibility of intratumoral administration for breast cancers and additional preclinical studies can determine the efficacy of the armored UCARTM1 in treatment of other metastatic solid tumors with a similar inhibitory TME. In conclusion, here we show strong preclinical evidence

in support of the intratumorally administered non-alloreactive UCARTM1$^{\Delta PD1/IL12;\ \Delta TGFBR2}$ in treatment of TNBCs with overall increased safety and potential to recognize metastasis.

Last, it is noteworthy that the intravenous treatment of UCARTM1$^{\Delta PD1/IL12;\ \Delta TGFBR2}$ synergistic effects of the attributes also confers high efficacy, reduced the number of circulating CAR T cells and serum IL-12, and extended survival in comparison to the TGFBR2^{WT} CAR T cell treatments and is not limited to the intratumoral methodology. It is fascinating to observe the synergy of both attributes and we hypothesize that multiple factors could contribute to this: (i) TGFBR2 inhibition has been previously associated with an increased effector function of T cells leading to a higher antitumor activity (74), which could be accompanied by the immunoinflammatory properties of IL-12; (ii) the reduction of proliferation could be contributing to a higher control of self-activation of CAR T cells and withdrawal of potential unspecific cytotoxic activity after killing the tumor; and (iii) a more controlled cell cycle progression could prevent potential hyperproliferation associated to self-autonomous effects of IL-12 in the absence of antigen stimulus (8). The reasons behind these mechanisms at the molecular level are not clear yet and future experiments based on multi-omics could reveal the specific interactions between both pathways. Another limitation of this study was that dose titration in the intravenous model for optimal therapeutic dose was not investigated because the remarkable responses we observed in the intratumoral administration shifted precedence. In sum, our study highlights the importance of combining different engineering strategies and CAR T cell administration methodologies to achieve an efficient tumor response in solid tumors with the potential to address metastatic sites in more advance disease. Thus, our findings pave the way to support the further development of multi-armored cell therapies, such as UCARTM1, offering potential therapeutic options to patients with metastatic breast cancer, which remains an unmet need.

MATERIALS AND METHODS
Primary cells, cell lines, and cell culture
Cryopreserved human peripheral blood mononuclear cells (PBMCs) were obtained from ALLCELLS (no. PB006F). PBMCs were cultured in CTS OpTmizer media (obtained from Gibco, no. A1048501) or X-Vivo media (Lonza, no. 02-053Q), containing IL-2 (Miltenyi Biotec, no. 130-097-748), human AB serum (Seralab, no. GEM-100-318), and CTS Immune Cell SR (Gibco, no. A2596101). Human T Cell TransAct (Miltenyi Biotec, no. 130-111-160) was used to activate T cells. Engineered cells were cryopreserved in fetal bovine serum (FBS) with 10% dimethyl sulfoxide (DMSO). HCC70-GFP and T47D-GFP were engineered from HCC70 cells [American Tissue Culture Collection (ATCC), no. CRL-2315] and T47D cells (ATCC, HTB-133) using an rLV encoding NanoLuc_T2A EGFP construct generated at GenScript and rLV produced at Flash Therapeutics, respectively, and sequences can be found in reference table S1 (79). Breast cancer cell lines, MDA-MB-468 (ATCC, HTB-132), MDA-MB-231 (ATCC, HTB-26), MCF7 (ATCC, HTB-22), HCC1937(ATCC, CRL-2336), HCC1395 (ATCC, CRL-2324), HCC38 (ATCC, CRL-2314), and the HEK293FT cell line (Invitrogen, no. R70007) were maintained in Dulbecco's modified Eagle's medium supplemented with 10% non–heat-inactivated FBS and 1% Pen/Strep in 5% CO_2 at 37°C, and human primary cervical epithelial cells (ATCC, PCS-480-011), bronchial/tracheal epithelial cells (ATCC,

PCS-300-010), and renal epithelial cells (ATCC, PCS-400-012) were maintained as described in the ATCC culture methods for each primary cell.

CAR construction

CARs directed against MUC1 were constructed by joining the respective single-chain variable fragments with the CD8α hinge/transmembrane domain (NP_001139345.1), 4-1BB (NP_001552.2), and CD3ζ (NP_932170.1) intracellular domains (tables S1 and S2). Codon optimization and gene synthesis were performed by Genscript. Coding sequences were cloned downstream of the EF1a promoter and upstream of the wood chuck hepatitis virus posttranscriptional regulatory element.

Lentivirus production, concentration, titration, and quantification

Viral particles were produced at Flash Therapeutics at small scale, and at research and development grade. Briefly, viral-derived vectors were produced by tri-transfection into 293T cells by using standard transfection methods. A total of 24 hours later, cells were washed with fresh medium. Viral supernatants were collected and filtered through 0.45-μm filters and subjected to ultrafiltration for purification and concentration of virus particles. Titers were estimated by qPCR 72 hours after transduction of HCT116 cells by serial dilution of viral supernatants. A GFP expression lentiviral vector was used as control in each plate of titration.

UCAR T cell generation and expansion

PBMCs were thawed (day 0), washed, resuspended, and cultured in full media containing CTS OpTmizer complete media (CTS OpTmizer + Supplement), 5% human AB serum (Gemini, no. 00-318), and IL-2 (20 ng/ml; Miltenyi Biotec, no. 130-097-743). One day later (day 1), cells were activated with Human T Cell TransAct (25 μl of beads/10^6 CD3$^+$ cells). The next day (day 2), 12 well untreated plates were coated for 1 hour at 37°C with retronectin (30 μg/ml; Takara Bio USA Inc., no. T100B) diluted in PBS and cells were transduced with M1, M2, M3, or M4 CAR rLV (Flash Therapeutics, 2×10^{10}, 7.2×10^9, 3×10^9, and 6.5×10^9 TU/ml, respectively) at a multiplicity of infection of 15. Cells were transduced at a concentration of 1.7×10^6 cells/ml in full media and cultured at 37°C in the presence of 5% CO_2 overnight. On day 3, cells were passaged in fresh full media. For cells carrying only the lentivirus expressing the CAR, cells were transferred after 2 to 3 days in culture to GREX6 devices (Wilson Wolf, 80240M) and grown for a total of 18 days.

For CAR T cells in Figs. 1 and 2: The steps of CAR T cell engineering described above were followed using X-vivo 15 media instead of the CTS OpTmizer. At day 7, cells were passaged to 1×10^6 cells/ml in fresh X-vivo 15 medium supplemented with 5% AB serum and IL-2 (20 ng/ml). Six hours later, cells were coelectroporated with mRNA encoding the right and the left arms of TRAC TALEN and PD1 TALEN using the AgilePulse technology as previously reported (11, 52). Cells were then incubated at 37°C for 15 min, with 5% CO_2. Next, cells were pelleted and resuspended with 200 μl of X-vivo 15 medium supplemented with 5% AB serum and IL-2 (20 ng/ml), and 50,000 vg per cell of IL-12 AAV6 was added to the cell suspension to be incubated at 30°C overnight. At day 8, cells were transferred to GREX6 devices for expansion and incubated at 37°C under 5% CO_2. Between days 8 and 18, 75% of the culture media was removed at day 13 and replaced with fresh medium containing IL-2, and fresh

IL-2 was added at days 11 and 15. Cells were grown until day 18, when they were collected and frozen at 50×10^6 to 100×10^6 cells/ml in FBS/10% DMSO.

For multi-engineered CAR T cells in Figs. 3 to 7: For cells carrying $TRAC^{KO}$, transfections were performed on day 3. Briefly, cells were washed once in Cytoporation buffer T (BTX Harvard Apparatus) and resuspended at a final concentration of 28×10^6 cells/ml in the same solution. A total of 5×10^6 cells were then mixed with 1 μg of mRNA encoding each TRAC TALEN arm in a final volume of 180 μl. The cellular suspension was transfected in a 0.4-cm-gap cuvette using Pulse Agile technology. The electroporation consisted of two 0.1-ms pulses at 800 V followed by four 0.2-ms pulses at 130 V. Electroporated cells were transferred to a 12-well plate containing 2 ml of prewarmed OpTmizer full media and incubated at 37°C for 15 min, with 5% CO_2 and then transferred to 30°C overnight. The next day, cells were seeded at a density of 1×10^6 cells/ml in complete OpTmizer media and cultured at 37°C with 5% CO_2. Cells were transfected with 2 μg of mRNA encoding each arm of both PD1 and TGFBR2 TALEN arms on day 7 using the Pulse agile program described above. Post-transfection, cells were spun down and resuspended at 8×10^6 cells/ml in complete OpTmizer media and 50,000 vg per cell of IL-12 AAV6 was added. Cells were incubated at 30°C overnight. The next day, the cells were resuspended in fresh full media and seeded in GREX6 at 2.5×10^6 cells/ml. On days 11 and 16, full media was refreshed, and on day 14, only IL-2 at 20 ng/ml was added. Cells were grown until day 18, when they were collected and frozen at 50×10^6 to 100×10^6 cells/ml in FBS/10% DMSO. All cells were counted using NucleoCounter NC-250 according to the manufacturer's protocol.

TCR depletion

To isolate TCRαβ-negative cells, CAR T cells were incubated with 1875 μl of TCRαβ biotin antibody (Miltenyi Biotec, 130-113-537) per 10^7 cells for 30 min in PBS with 0.5% FBS and 2 mM ethylenediaminetetraacetic acid (EDTA). After that, cells were washed in PBS with 0.5% FBS and 2 mM EDTA and posteriorly incubated with 3.75 μl of anti-biotin magnetic bead per 10^7 cells for 30 min (Miltenyi Biotec, 130-090-485) at room temperature. After washing with PBS with 0.5% FBS and 2 mM EDTA, cells were resuspended in 500 μl of PBS with 0.5% FBS and 2 mM EDTA and purified using an LD column (Miltenyi Biotec, 130-042-901) following the manufacturer's protocol.

Targeted PCR

Genomic DNA (100 μg) was used per reaction in a 50-l reaction with Phusion High-Fidelity PCR Master Mix (NEB). The PCR condition was set to 1 cycle of 30 s at 98°C; 30 cycles of 10 s at 98°C, 30 s at 60°C, 30 s at 72°C; 1 cycle of 5 min at 72°C; hold at 4°C. Primers for PDCD1 locus were 5′-CTACACGACGCTCTTCCGATCTCAGCTTCTCCAACACATCGG-3′ and 5′-GTGACTGGAGTTCAGACGTGTGCTCTTCCGATCTAATTTCCCCAGGTGCAGGACAGA-3′, and those for TGFBR2 locus were 5′-CTACACGACGCTCTTCCGATCTTCATCCTGGAAGATGACCGC-3′ and 5′-GTGACTGGAGTTCAGACGTGTGCTCTTCCGATCTAATTCAGCCAGTATTGTTTCCCCA-3′. The PCR product was then purified with Omega NGS beads (1:1.2 ratio) and eluted into 30 μl of 10 mM tris buffer, pH 7.4. The second PCR that incorporates NGS indices was then performed on the purified product from the first PCR. The first PCR product (15 μl) was set in a 50-μl reaction with Phusion

High-Fidelity PCR Master Mix (NEB). The PCR condition was set to 1 cycle of 30 s at 98°C; 8 cycles of 10 s at 98°C, 30 s at 62°C, 30 s at 72°C; 1 cycle of 5 min at 72°C; hold at 4°C. Primers used were 5′-AATGATACGGCGACCACCGAGATCTACACTCTTTCCCTA-CACGACGCTCTTCCGATCT-3′ and 5′-CAAGCAGAAGACGGCATACGAGAT\<barcode>GTGACTGGAGTTC-3' Purified PCR products were sequenced on MiSeq (Illumina) on a 2 × 250 nano V2 cartridge.

ddPCR to measure IL-12 insertions at the *PDCD1* locus

Cell pellets were harvested from bulk engineered PBMCs 11 days after the last editing event (18 days since the initiation of culture). Genomic DNA was extracted using the Mag-Bind Blood & Tissue DNA HDQ 96 Kit (Omega Bio-Tek, Norcross, GA, USA) according to the manufacturer's protocols on the KingFisher Flex purification system (ThermoFisher Scientific). A multiplex digital droplet PCR (ddPCR) assay was performed to measure gene editing rates, where one primer/probe set was designed to amplify a reference gene (*CCR5*) and another set amplified the integrated cassette at the desired genomic location using our PCR approach. For reference gene *CCR5*, primer sequences were 5′-AAATAAGCT-GCCTTGAGCC-3′ and 5′-TGTTGCACTCTCCACAACTT-3′ and a HEX-tagged 5′-TCCCTTCGTTGCTTCCTGCTGACA-3′ probe, and for PD1-inserted IL-12, 5′-GACAGCAAGGGGGAGGAT-3′ and 5′-TCTGCCCTTCTCTCTGGAAG-3′, and a FAM-tagged 5′-CAGCATGCCTGCTATTGTCTT-3′ probe with an internal ZEN quencher. A total of 40 to 100 ng of gDNA was combined with 22.5 pmol each forward and reverse target primer, 22.5 pmol each forward and reverse reference primer, 62.5 pmol each target FAM probe and reference HEX probe, and 1× ddPCRSupermix for Probes without dUTP (Bio-Rad Laboratories, Hercules, CA, USA), in a 25-μl reaction. Droplets were generated on a QX200 Droplet Generator (Bio-Rad Laboratories) according to the manufacturer's protocol. Droplets were amplified using a Bio-Rad PCR thermocycler using the following PCR conditions: 95°C for 10 min, 40 cycles of 94°C for 30 s, 58°C for 30 s, and 60°C for 2 min, followed by 98°C for 10 min and 4°C until droplet analysis. Droplets were analyzed on a QX200 Droplet Reader (Bio-Rad Laboratories) using the QuantaSoft Software (Bio-Rad Laboratories) to detect FAM and HEX fluorescence positive and negative droplets according to the manufacturer's protocol. Control samples with non-template control and mock-treated samples were included.

In vitro antitumor activity assays

At day 0, target cells of either T47D-NanoLuc-GFP or HCC70-NanoLuc-GFP were plated in a flat-bottom 96-well plate at a density of 10,000 target cells per well. Cells were plated in their respective complete medium. At day 1, medium was removed from target cells and CAR T cells or NTD cells were added to target cells at a 1:1, 1:2.5, or 1:5 CAR$^+$ E:T ratio in X-Vivo medium supplemented with 5% AB serum. Target cells were cocultured with CAR T cells or the NTD control cells for 48 hours in an incubator set at 37°C, 5% CO$_2$. Subsequently, NanoLuciferase signal was developed with the following protocol: Medium was removed, wells were washed once with 100 μl of PBS and then incubated with 0.026% Triton X-100 in PBS for 2 min with vortexing. The plate was spun down at 2000 rpm for 3 min. A total of 20 μl of lysate was diluted in 30 μl of PBS, mixed with 50 μl of Nano-Glo substrate (Promega, no. N1110), vortexed for 1 min, and the luminescence was next read. Percent specific lysate was calculated using the following equation: % Lysis = [1 − (Target + scFv UCART)/(Target + NTD UCART)]*100. When indicated, TGFB1 (R&D Systems, no. 240B010) was added at a concentration of 5 ng/ml.

For Incucyte analysis: At day 0, 10,000 target T47D-NanoLuc-GFP cells were plated per well in a flat-bottom 96-well plate (as triplicates) in their respective complete medium. At day 1, media was refreshed and CAR T cells or NTD cells were added with 3:1 E:T ratio (some wells were cultured without CAR T cells to assess baseline growth of the tumor cells/GFP objects). The Incucyte (Sartorius) fluorescence imaging was done every 30 min for 45 hours and GFP$^+$ object count per well was analyzed using the Incucyte software (Zoom 2016A Rev1 GUI).

In vitro proliferation assays

Wells of the 24-well plate were coated first with 1 ml streptavidin (Jackson Immunoresearch, no. 016-000-113) at 5 μg/ml concentration for 2 hours at 37°C, and then with 1 ml of naked MUC1 recombinant protein (5 μg/ml; peptide sequence: HGVTSAP-DTRPAPGSTAPPA) for 2 hours. Wells without recombinant protein were also prepared. The wells were washed with PBS in between coatings and before the addition of CAR T cells. CAR T cells were thawed in CTS OpTmizer complete media and 10% human AB serum, and 1×10^6 cells were added in each coated well resuspended in CTS OpTmizer complete media, 10% human AB serum, and IL-2 (70 UI/ml). When indicated, TGFB1 (R&D Systems, no. 240B010) was added to the culture medium at a concentration of 5 ng/ml. Cells were counted, and coating and the media were refreshed on days 0, 4, 6, 8, and 11.

scFv-fc production

scFv proteins for tissue microarray (TMA) and healthy primary cell studies were synthesized at Lakepharma (now Curia). Briefly, scFv sequences were synthesized and cloned into a mammalian expression vector to produce scFv proteins conjugated with murine IgG1-Fc. Tuna293 (for M3) or CHO (for M1 and M4) cells were transfected with the constructs and 0.1 liters of transient production of protein was generated. After cell harvesting, produced proteins were purified with protein A affinity purification and lastly stored in 100 mM Hepes, 100 mM NaCl, and 50 mM NaOAc, pH 6.0, buffer.

Tissue microarray

Tissue microarray was purchased at US Biomax (catalog number BR1902). For IHC, after dewaxing the FFPE sections in consecutive baths: xylene (2 min), ethanol 100°C (1 min), then ethanol 96°C (1 min) and lastly ethanol 70°C (1 min), the slides were washed in Millipore water (1 min), then washed in reaction buffer (3 min at least), and then uploaded in the Discovery XT2 instrument and an automated procedure was performed. Briefly, after a second step of dewaxing, the slides were incubated with a solution of CC2 (Ventana no. 760-107) for 32 min, the sections were then incubated with the primary antibodies prepared in Antibody diluent (Ventana, no. 760-108) for 60 min at 37°C, and the detection system OmniMap anti-Ms HRP (Ventana, no. 760-4310) was applied for 16 min, the sections were stained with Hematoxylin II (Ventana, no. 790-2208) and bluing reagent (Ventana, no. 760-2037) (2 × 4 min), thoroughly washed in soap water followed by tap water and dehydrated, and lastly, all slides were mounted. A concentration of 3 μg/ml for M1 and M3,

and 9 μg/ml for M4 and negative control was used for the staining in the TMA.

IL-12, IFNG, and TGFB1 ELISAs

IL-12 levels were measured with Quantikine ELISA Human IL-12 p70 Immunoassay (R&D Systems, no. D1200) using 30 μl of blood. IFNG levels in blood serum were determined using the Human IFN-Gamma Quantikine Kit (R&D Systems, no. SIF50) following the manufacturer's instructions using 1 μl of blood. Tumors in the mammary fat pad and normal mouse mammary fat pads (MFP, $N = 5$) were digested as described in the "Tissue processing and flow cytometry for in vivo samples" section below, cells were pelleted, and 200 μl of the supernatants was used in the TGFB1 ELISA. TGFB1 levels in tumor and MFP serum were determined using the Human/Mouse/Rat/Porcine/Canine TGFB1 Quantikine Kit (R&D Systems, no. DB100B) following the manufacturer's instructions. The TGFB1 levels of the tumors were normalized to the TGFB1 levels detected at baseline in the MFP, to assess the TGFB1 secreted by the HCC70 tumor cells.

Mice and animal procedures

All procedures involving animals were approved by The MISPRO Institutional Animal Care and Use Committee and were performed in accordance with the guidelines of the PHS (Public Health Service) Policy on Humane Care and Use of Laboratory Animals, OLAW (Office of Laboratory Animal Welfare), and the USDA (United States Department of Agriculture) AWA (Animal Welfare Act), with study approval number 2022-CEL-03. Experimental/control animals were cohoused. All experiments were performed on 6- to 8-week-old female NOD.Cg-Prkdcscid Il2rgtm1Wjl/SzJ (NSG) mice obtained from the Jackson Laboratory (stock no. 005557). Animals were housed in SPF animal facility. HCC70 tumor cells, in 50 μl of ice-cold PBS:Matrigel (1:1), were injected into the MFP of 6- to 8-week-old female NSG mice anesthetized briefly with isoflurane. Mice were randomly enrolled into the study once tumor volume reached ~50, 100, or 450 mm^3 based on the model; each cohort had similar average starting tumor volume pre-CAR T cell treatment. Initial experiments with intravenous treatment were started when tumors reached 50 mm^3. On the basis of the results of the TGFB1 levels, tumor size was increased to 450 mm^3. For CAR T cell treatment, tumor-bearing mice received a single dose unless indicated otherwise. The CAR T cell doses varied between experiments ranging from 1×10^6 to 15×10^6 as indicated in the figures in 100 μl of PBS for both intratumoral and intravenous models. The intratumoral injections were done using a 0.5-ml insulin needle, targeting the middle of the tumor with a single injection while animals were under anesthesia with isoflurane. The tumors smaller than 2 to 3 mm were considered palpable, until no mass was left to palpate. Measurable tumors were defined as tumors that are larger than 3 mm and could be measured with the caliper. Tumor clearance was identified on a histological level when no tumor cells were detected. Tumor volume, animal weight, and health were measured every 5 to 7 days, and tumor volume was calculated using the formula [length × (width)^2/2]. Tumors not implanted in MFP were excluded from the study. IL-2 (Miltenyi Biotec, no. 130-097-745) was injected intratumorally using an insulin needle, 35,000 IU in 100 μl per mouse for the indicated experiment (Fig. 4G). Animal health and humane end point criteria were determined upon (i) weight loss greater than or equal to 20% from baseline; (ii) abnormal gait, paralysis, or inability to ambulate properly; (iii) respiratory distress/labored breathing; (iv) lethargy or persistent recumbency; (v) loss of righting reflex or other abnormal neurological behaviors; and (vi) tumor volume reaching 2 cm in any one direction (for the one-tumor model) and a total of 2 cm (for the two-tumor model). The method for euthanasia was CO_2 asphyxiation followed by cervical dislocation. All schematics were created with BioRender.com.

Histology and IHC

Tumors, spleens, and mammary glands were fixed in 10% buffered formalin (Thermo Fisher Scientific) overnight and washed and stored in 70% ethanol. Histology, IHC, and trichrome staining were performed by HistoWiz Inc. (histowiz.com/) using a standard operating procedure and fully automated workflow. Samples were processed, embedded in paraffin, and sectioned at 4 μm. Immunohistochemistry was performed on a Bond Rx autostainer (Leica Biosystems) with enzyme treatment (1:1000) using standard protocols. Antibodies used were α-hCD45 (Abcam, no. ab40763), hCD8A (LS-Bio, no. LS-B3914), GFP (Abcam, no. ab183734), and PD-L1 (CST, no. 13684). Bond Polymer Refine Detection (Leica Biosystems) was used according to the manufacturer's protocol. After staining, sections were dehydrated and film coverslipped using a TissueTek-Prisma and Coverslipper (Sakura). Whole slide scanning (40×) was performed on an Aperio AT2 (Leica Biosystems).

Tissue processing and flow cytometry for in vivo samples

For tumor samples: Tumor tissue was chopped finely with a razor, placed in 1 ml of Acutase (BioLegend, no. 4232201), and incubated at 37°C for 1 h with agitation every 15 min. Digested tumor suspension was passed through a 100-μm strainer (Corning) and washed with PBS. Cells were pelleted via $500g \times 5$ min and stained for flow cytometry as described below. For spleen samples: Mouse spleens were processed by crushing the spleen in 5 ml of PBS and 2% FBS. Cell suspension was spun at $300g$ for 10 min. Cell pellet was suspended in 1× RBC lysis buffer (eBioscience, no. 00-4300-54) for 5 min at room temperature and then filtered through a 70-μm strainer (Corning). Cells were pelleted and stained for flow cytometry as described below. For peripheral blood samples: 15 or 20 μl of blood was collected in capillary tubes (Thermo Fisher Scientific, no. 22-030-403) and pelleted with centrifugation at $500g$ for 5 min. Cell pellet was suspended in 1× RBC lysis buffer (eBioscience, no. 00-4300-54) for 5 min at room temperature. RBC lysis was repeated if the pellet remained red. Cells were pelleted via $500g \times 5$ min and stained for flow cytometry as described below. For serum: Blood samples were collected, centrifuged for 10 min at 12,000 rpm and the supernatant/serum was removed and stored at −80°C.

For in vitro cell cultures, and all processed mice tissue: Cells were spun down in a U-bottom 96-well plate and were first stained with Fixable Viability Dye eFluor 780 (eBiosciences, no. 50-69-66, 1:1000) according to the manufacturer's instructions. Cells were then washed with FACS (fluorescence-activated cell sorting) buffer (2% FBS in PBS) and stained with antibodies diluted in FACS buffer for 30 min in the dark at 4°C. For antibodies that required secondary antibodies, primary antibody staining was done as described and the cells were washed and stained with the secondary antibody for 20 min in the dark at 4°C. Cells were washed again with FACS buffer, spun at $300g$ for 5 min, and resuspended in fix buffer (4% paraformaldehyde in 2% FBS in PBS, 150 μl per well). For intracellular staining, BD Cytofix/Cytoperm Fixation/Permeabilization Kit

was used (BD, no. 554714). Cells were resuspended in permeabilization/fixation buffer and incubated for 20 min at 4°C and then washed and incubated with Perm/Wash buffer containing primary antibody for 30 min at 4°C. Next, cells were washed again, and stained with secondary antibody in Perm/Wash buffer for 30 min at 4°C. Last, cells were washed with Perm/Wash buffer and resuspended in fix buffer described above. Refer to table S3 for all antibodies used. Data collection was performed on a NovoCyte Penteon flow cytometer (Agilent), and data were analyzed using FlowJo V.10.6.1 (Treestar) or NovoExpress V.1.5.6 (Agilent).

Statistical analysis

For statistical analysis, GraphPad Prism 9.4 was used. Two-way analysis of variance (ANOVA) or mixed-effects analysis was performed for comparisons over time for tumor growth. The log-rank Mantel-Cox test was used for survival curves. Unpaired t test or ordinary one-way ANOVA was used for all other analysis. P value was indicated as follows $*P < 0.05$, $**P \leq 0.01$, $***P \leq 0.001$, and $****P \leq 0.0001$.

Supplementary Materials

The PDF file includes:
Figs. S1 to S7
Tables S1 to S3
Legend for data S1

Other Supplementary Material for this manuscript includes the following:
Data S1

REFERENCES AND NOTES

1. N. Harbeck, F. Penault-Llorca, J. Cortes, M. Gnant, N. Houssami, P. Poortmans, K. Ruddy, J. Tsang, F. Cardoso, Breast cancer. *Nat. Rev. Dis. Primers.* **5**, 66 (2019).
2. P. Kumar, R. Aggarwal, An overview of triple-negative breast cancer. *Arch. Gynecol. Obstet.* **293**, 247–269 (2016).
3. G. Bianchini, C. De Angelis, L. Licata, L. Gianni, Treatment landscape of triple-negative breast cancer—Expanded options, evolving needs. *Nat. Rev. Clin. Oncol.* **19**, 91–113 (2022).
4. S. Dees, R. Ganesan, S. Singh, I. S. Grewal, Emerging CAR-T cell therapy for the treatment of triple-negative breast cancer. *Mol. Cancer Ther.* **19**, 2409–2421 (2020).
5. R. C. Sterner, R. M. Sterner, CAR-T cell therapy: Current limitations and potential strategies. *Blood Cancer J.* **11**, 69 (2021).
6. A. Daei Sorkhabi, L. Mohamed Khosroshahi, A. Sarkesh, A. Mardi, A. Aghebati-Maleki, L. Aghebati-Maleki, B. Baradaran, The current landscape of CAR T-cell therapy for solid tumors: Mechanisms, research progress, challenges, and counterstrategies. *Front. Immunol.* **14**, 1113882 (2023).
7. L. Tang, S. Pan, X. Wei, X. Xu, Q. Wei, Arming CAR-T cells with cytokines and more: Innovations in the fourth-generation CAR-T development. *Mol. Ther.* **31**, 3146–3162 (2023).
8. A. Smole, A. Benton, M. A. Poussin, M. A. Eiva, C. Mezzanotte, B. Camisa, B. Greco, P. Sharma, N. G. Minutolo, F. Gray, A. S. Bear, M. L. Baroja, C. Cummins, C. Xu, F. Sanvito, A. L. Goldgewicht, T. Blanchard, A. Rodriguez-Garcia, M. Klichinsky, C. Bonini, C. H. June, A. D. Posey, G. P. Linette, B. M. Carreno, M. Casucci, D. J. Powell, Expression of inducible factors reprograms CAR-T cells for enhanced function and safety. *Cancer Cell* **40**, 1470–1487.e7 (2022).
9. R. A. Brog, S. L. Ferry, C. T. Schiebout, C. M. Messier, W. J. Cook, L. Abdullah, J. Zou, P. Kumar, C. L. Sentman, H. R. Frost, Y. H. Huang, Superkine IL-2 and IL-33 armored CAR T cells reshape the tumor microenvironment and reduce growth of multiple solid tumors. *Cancer Immunol. Res.* **10**, 962–977 (2022).
10. S. K. Kim, L. Barron, C. S. Hinck, E. M. Petrunak, K. E. Cano, A. Thangirala, B. Iskra, M. Brothers, M. Vonberg, B. Leal, B. Richter, R. Kodali, A. B. Taylor, S. Du, C. O. Barnes, T. Sulea, G. Calero, P. J. Hart, M. J. Hart, B. Demeler, A. P. Hinck, An engineered transforming growth factor β (TGF-β) monomer that functions as a dominant negative to block TGF-β signaling. *J. Biol. Chem.* **292**, 7173–7188 (2017).
11. M. Sachdeva, B. W. Busser, S. Temburni, J. Jahangiri, A. S. Gautron, A. Maréchal, A. Juillerat, A. Williams, S. Depil, P. Duchateau, L. Poirot, J. Valton, Repurposing endogenous immune pathways to tailor and control chimeric antigen receptor T cell functionality. *Nat. Commun.* **10**, 5100 (2019).
12. D. W. Kufe, Mucins in cancer: Function, prognosis and therapy. *Nat. Rev. Cancer* **9**, 874–885 (2009).
13. M. Movahedin, T. M. Brooks, N. T. Supekar, N. Gokanapudi, G. J. Boons, C. L. Brooks, Glycosylation of MUC1 influences the binding of a therapeutic antibody by altering the conformational equilibrium of the antigen. *Glycobiology* **27**, 677–687 (2017).
14. P. A. Burke, J. P. Gregg, B. Bakhtiar, L. A. Beckett, G. L. Denardo, H. Albrecht, R. W. De Vere White, S. J. De Nardo, Characterization of MUC1 glycoprotein on prostate cancer for selection of targeting molecules. *Int. J. Oncol.* **29**, 49–55 (2006).
15. S. Nath, P. Mukherjee, MUC1: A multifaceted oncoprotein with a key role in cancer progression. *Trends Mol. Med.* **20**, 332–342 (2014).
16. A. Siroy, F. W. Abdul-Karim, J. Miedler, N. Fong, P. Fu, H. Gilmore, J. Baar, MUC1 is expressed at high frequency in early-stage basal-like triple-negative breast cancer. *Hum. Pathol.* **44**, 2159–2166 (2013).
17. M. Alam, H. Rajabi, R. Ahmad, C. Jin, D. Kufe, Targeting the MUC1-C oncoprotein inhibits self-renewal capacity of breast cancer cells. *Oncotarget* **5**, 2622–2634 (2014).
18. L. Keren, M. Bosse, D. Marquez, R. Angoshtari, S. Jain, S. Varma, S. R. Yang, A. Kurian, D. Van Valen, R. West, S. C. Bendall, M. Angelo, A structured tumor-immune microenvironment in triple negative breast cancer revealed by multiplexed ion beam imaging. *Cell* **174**, 1373–1387 (2018).
19. Y. Jiang, Y. Li, B. Zhu, T-cell exhaustion in the tumor microenvironment. *Cell Death Dis.* **6**, e1792 (2015).
20. G. López-Cantillo, C. Urueña, B. A. Camacho, C. Ramírez-Segura, CAR-T cell performance: How to improve their persistence? *Front. Immunol.* **13**, 878209 (2022).
21. D. L. Porter, W.-T. Hwang, N. V. Frey, S. F. Lacey, P. A. Shaw, A. W. Loren, A. Bagg, K. T. Marcucci, A. Shen, V. Gonzalez, D. Ambrose, S. A. Grupp, A. Chew, Z. Zheng, M. C. Milone, B. L. Levine, J. J. Melenhorst, C. H. June, Chimeric antigen receptor T cells persist and induce sustained remissions in relapsed refractory chronic lymphocytic leukemia. *Sci. Transl. Med.* **7**, 303ra139 (2015).
22. K. G. Nguyen, M. R. Vrabel, S. M. Mantooth, J. J. Hopkins, E. S. Wagner, T. A. Gabaldon, D. A. Zaharoff, Localized interleukin-12 for cancer immunotherapy. *Front. Immunol.* **11**, 575597 (2020).
23. B. J. P. Leonard, M. L. Sherman, G. L. Fisher, L. J. Buchanan, G. Larsen, M. B. Atkins, J. A. Sosman, J. P. Dutcher, N. J. Vogelzang, J. L. Ryan, Effects of single-dose interleukin-12 exposure on interleukin-12-associated toxicity and interferon-gamma production. *Blood* **90**, 2541–2548 (1997).
24. H. J. Pegram, J. C. Lee, E. G. Hayman, G. H. Imperato, T. F. Tedder, M. Sadelain, R. J. Brentjens, Tumor-targeted T cells modified to secrete IL-12 eradicate systemic tumors without need for prior conditioning. *Blood* **119**, 4133–4141 (2012).
25. L. Zhang, R. A. Morgan, J. D. Beane, Z. Zheng, M. E. Dudley, S. H. Kassim, A. V. Nahvi, L. T. Ngo, R. M. Sherry, G. Q. Phan, M. S. Hughes, U. S. Kammula, S. A. Feldman, M. A. Toomey, S. P. Kerkar, N. P. Restifo, C. Y. Yang, S. A. Rosenberg, Tumor-infiltrating lymphocytes genetically engineered with an inducible gene encoding interleukin-12 for the immunotherapy of metastatic melanoma. *Clin. Cancer Res.* **21**, 2278–2288 (2015).
26. Y. Liu, S. Di, B. Shi, H. Zhang, Y. Wang, X. Wu, H. Luo, H. Wang, Z. Li, H. Jiang, Armored inducible expression of IL-12 enhances antitumor activity of Glypican-3–targeted chimeric antigen receptor–engineered T cells in hepatocellular carcinoma. *J. Immunol.* **203**, 198–207 (2019).
27. D. Chinnasamy, Z. Yu, S. P. Kerkar, L. Zhang, R. A. Morgan, N. P. Restifo, S. A. Rosenberg, Local delivery of interleukin-12 using T cells targeting VEGF receptor-2 eradicates multiple vascularized tumors in mice. *Clin. Cancer Res.* **18**, 1672–1683 (2012).
28. M. Chmielewski, C. Kopecky, A. A. Hombach, H. Abken, IL-12 release by engineered T cells expressing chimeric antigen receptors can effectively muster an antigen-independent macrophage response on tumor cells that have shut down tumor antigen expression. *Cancer Res.* **71**, 5697–5706 (2011).
29. A. Alsaieedi, A. Holler, G. Bendle, H. J. Stauss, Safety and efficacy of Tet-regulated IL-12 expression in cancer-specific T cells. *Oncoimmunology* **8**, 1542917 (2019).
30. S. Champiat, L. Tselikas, S. Farhane, T. Raoult, M. Texier, E. Lanoy, C. Massard, C. Robert, S. Ammari, T. de Baere, A. Marabelle, Intratumoral immunotherapy: From trial design to clinical practice. *Clin. Cancer Res.* **27**, 665–679 (2021).
31. W. X. Hong, S. Haebe, A. S. Lee, C. B. Westphalen, J. A. Norton, W. Jiang, R. Levy, Intratumoral immunotherapy for early-stage solid tumors. *Clin. Cancer Res.* **26**, 3091–3099 (2020).
32. J. Yu, X. Wu, J. Yan, H. Yu, L. Xu, Z. Chi, X. Sheng, L. Si, C. Cui, J. Dai, M. Ma, T. Xu, Y. Kong, J. Guo, Anti-GD2/4-1BB chimeric antigen receptor T cell therapy for the treatment of Chinese melanoma patients. *J. Hematol. Oncol.* **11**, 1 (2018).
33. I. Melero, E. Castanon, M. Alvarez, S. Champiat, A. Marabelle, Intratumoural administration and tumour tissue targeting of cancer immunotherapies. *Nat. Rev. Clin. Oncol.* **18**, 558–576 (2021).
34. C. E. Brown, B. Aguilar, R. Starr, X. Yang, W. C. Chang, L. Weng, B. Chang, A. Sarkissian, A. Brito, J. F. Sanchez, J. R. Ostberg, M. D'Apuzzo, B. Badie, M. E. Barish, S. J. Forman, Optimization of IL13Rα2-targeted chimeric antigen receptor T cells for improved anti-tumor efficacy against glioblastoma. *Mol. Ther.* **26**, 31–44 (2018).
35. C. R. Shyr, L. C. Liu, H. S. Chien, C. P. Huang, Immunotherapeutic agents for intratumoral immunotherapy. *Vaccines* **11**, 1717 (2023).

36. A. M. Kieliszek, D. Mobilio, D. Upreti, D. Bloemberg, L. Escudero, J. M. Kwiecien, Z. Alizada, K. Zhai, P. Ang, S. C. Chafe, P. Vora, C. Venugopal, S. K. Singh, Intratumoral delivery of chimeric antigen receptor T cells targeting CD133 effectively treats brain metastases. *Clin. Cancer Res.* **30**, 554–563 (2024).

37. S. Papa, A. Adami, M. Metoudi, R. Beatson, M. S. George, M. Achkova, E. Williams, S. Arif, F. Reid, M. Elstad, N. Beckley-Hoelscher, A. Douri, M. Delord, M. Lyne, D. Shivapatham, C. Fisher, A. Hope, S. Gooljar, A. Mitra, L. Gomm, C. Morton, R. Henley-Smith, S. Thavaraj, A. Santambrogio, C. Andoniadou, S. Allen, V. Gibson, G. J. R. Cook, A. C. Parente-Pereira, D. M. Davies, F. Farzaneh, A. Schurich, T. Guerrero-Urbano, J. P. Jeannon, J. Spicer, J. Maher, Intratumoral pan-ErbB targeted CAR-T for head and neck squamous cell carcinoma: Interim analysis of the T4 immunotherapy study. *J. Immunother. Cancer* **11**, e007162 (2023).

38. C. Zuo, Y. Zou, G. Gao, L. Sun, B. Yu, Y. Guo, X. Wang, M. Han, Photothermal combined with intratumoral injection of annonaceous acetogenin nanoparticles for breast cancer therapy. *Colloids Surf. B Biointerfaces* **213**, 112426 (2022).

39. C. Slingluff, I. Mauldin, E. Gaughan, P. Dillon, M. Opyrchal, I. Puzanov, M. Kruse, B. Gastman, P. Friedlander, T. Marron, K. Aufiero, M. Macri, P. Schwarzenberger, T. Ricciardi, A. Ryan, R. Venhaus, M. Saxena, N. Edmonds, N. Bhardwaj, 337 Intratumoral immune therapy for recurrent breast cancer with polyICLC, and tremelimumab combined with systemic durvalumab. *J. Immunother. Cancer* **9**, 10.1136/jitc-2021-SITC2021.337 (2021).

40. M. Telli, B. Devitt, K. Cuff, S. Vinayak, R. Nanda, A. J. Montero, R. Hui, D. A. Canton, C. Twitty, S. Xie, D. Bannavong, B. O'Keeffe, S. Aung, R. Joshi, Abstract OT2-01-03: Trial in progress: Phase 2 study of intratumoral plasmid interleukin-12 (tavokinogene telseplasmid; TAVO™) plus electroporation in combination with pembrolizumab with or without chemotherapy in patients with inoperable locally advanced or metastatic triple-negative breast cancer (KEYNOTE-890/OMS-I141). *Cancer Res.* **82**, 10.1158/1538-7445. SABCS21-OT2-01-03 (2022).

41. A. Globerson-Levin, T. Waks, Z. Eshhar, Elimination of progressive mammary cancer by repeated administrations of chimeric antigen receptor-modified T cells. *Mol. Ther.* **22**, 1029–1038 (2014).

42. H. Soliman, D. Hogue, H. Han, B. Mooney, R. Costa, M. C. Lee, B. Niell, A. Williams, A. Chau, S. Falcon, A. Soyano, A. Armaghani, N. Khakpour, R. J. Weinfurtner, S. Hoover, J. Kiluk, C. Laronga, M. Rosa, H. Khong, B. Czerniecki, Oncolytic T-VEC virotherapy plus neoadjuvant chemotherapy in nonmetastatic triple-negative breast cancer: A phase 2 trial. *Nat. Med.* **29**, 450–457 (2023).

43. J. Tchou, Y. Zhao, B. L. Levine, P. J. Zhang, M. M. Davis, J. J. Melenhorst, I. Kulikovskaya, A. L. Brennan, X. Liu, S. F. Lacey, A. D. Posey Jr., A. D. Williams, A. So, J. R. Conejo-Garcia, G. Plesa, R. M. Young, S. McGettigan, J. Campbell, R. H. Pierce, J. M. Matro, A. M. DeMichele, A. S. Clark, L. J. Cooper, L. M. Schuchter, R. H. Vonderheide, C. H. June, Safety and efficacy of intratumoral injections of chimeric antigen receptor (CAR) T cells in metastatic breast cancer. *Cancer Immunol. Res.* **5**, 1152–1161 (2017).

44. K. Zhang, H. Chen, F. Li, S. Huang, F. Chen, Y. Li, Bright future or blind alley? CAR-T cell therapy for solid tumors. *Front. Immunol.* **14**, 1045024 (2023).

45. S. M. Albelda, CAR T cell therapy for patients with solid tumours: Key lessons to learn and unlearn. *Nat. Rev. Clin. Oncol.* **21**, 47–66 (2024).

46. E. H. J. Lee, J. P. Murad, L. Christian, J. Gibson, Y. Yamaguchi, C. Cullen, D. Gumber, A. K. Park, C. Young, I. Monroy, J. Yang, L. A. Stern, L. N. Adkins, G. Dhapola, B. Gittins, W. C. Chang, C. Martinez, Y. Woo, M. Cristea, L. Rodriguez-Rodriguez, J. Ishihara, J. K. Lee, S. J. Forman, L. D. Wang, S. J. Priceman, Antigen-dependent IL-12 signaling in CAR T cells promotes regional to systemic disease targeting. *Nat. Commun.* **14**, 4737 (2023).

47. J. Valton, V. Guyot, B. Boldajipour, C. Sommer, T. Pertel, A. Juillerat, A. Duclert, B. J. Sasu, P. Duchateau, L. Poirot, A versatile safeguard for chimeric antigen receptor T-cell immunotherapies. *Sci. Rep.* **8**, 8972 (2018).

48. Y. Geng, T. Takatani, K. Yeh, J. W. Hsu, M. R. King, Targeting underglycosylated MUC1 for the selective capture of highly metastatic breast cancer cells under flow. *Cell. Mol. Bioeng.* **6**, 148–159 (2013).

49. W. Song, E. S. Delyria, J. Chen, W. Huang, J. S. Lee, E. A. Mittendorf, N. Ibrahim, L. G. Radvanyi, Y. Li, H. Lu, H. Xu, Y. Shi, L. X. Wang, J. A. Ross, S. P. Rodrigues, I. C. Almeida, X. Yang, J. Qu, N. S. Schocker, K. Michael, D. Zhou, MUC1 glycopeptide epitopes predicted by computational glycomics. *Int. J. Oncol.* **41**, 1977–1984 (2012).

50. Y. Yoshimura, K. Denda-Nagai, Y. Takahashi, I. Nagashima, H. Shimizu, T. Kishimoto, M. Noji, S. Shichino, Y. Chiba, T. Irimura, Products of chemoenzymatic synthesis representing MUC1 tandem repeat unit with T-, ST- or STn-antigen revealed distinct specificities of anti-MUC1 antibodies. *Sci. Rep.* **9**, 16641 (2019).

51. S. Naito, T. Takahashi, J. Onoda, S. Uemura, N. Ohyabu, H. Takemoto, S. Yamane, I. Fujii, S. I. Nishimura, Y. Numata, Generation of novel anti-MUC1 monoclonal antibodies with designed carbohydrate specificities using MUC1 glycopeptide library. *ACS Omega* **2**, 7493–7505 (2017).

52. L. Poirot, B. Philip, C. Schiffer-Mannioui, D. Le Clerre, I. Chion-Sotinel, S. Derniame, P. Potrel, C. Bas, L. Lemaire, R. Galetto, C. Lebuhotel, J. Eyquem, G. W. K. Cheung, A. Duclert, A. Gouble, S. Arnould, K. Peggs, M. Pule, A. M. Scharenberg, J. Smith, Multiplex genome-edited T-cell manufacturing platform for "off-the-shelf" adoptive T-cell immunotherapies. *Cancer Res.* **75**, 3853–3864 (2015).

53. Y. Lv, D. Lv, X. Lv, P. Xing, J. Zhang, Y. Zhang, Immune cell infiltration-based characterization of triple-negative breast cancer predicts prognosis and chemotherapy response markers. *Front. Genet.* **12**, 616469 (2021).

54. M. P. Hwang, R. J. Fecek, T. Qin, W. J. Storkus, Y. Wang, Single injection of IL-12 coacervate as an effective therapy against B16-F10 melanoma in mice. *J. Control. Release* **318**, 270–278 (2020).

55. S. J. Priceman, D. Tilakawardane, B. Jeang, B. Aguilar, J. P. Murad, A. K. Park, W. C. Chang, J. R. Ostberg, J. Neman, R. Jandial, J. Portnow, S. J. Forman, C. E. Brown, Regional delivery of chimeric antigen receptor-engineered T cells effectively targets HER2 + breast cancer metastasis to the brain. *Clin. Cancer Res.* **24**, 95–105 (2018).

56. P. Sridhar, F. Petrocca, Regional delivery of chimeric antigen receptor (CAR) T-cells for cancer therapy. *Cancers* **9**, 92 (2017).

57. P. Vora, C. Venugopal, S. K. Salim, N. Tatari, D. Bakhshinyan, M. Singh, M. Seyfrid, D. Upreti, S. Rentas, N. Wong, R. Williams, M. A. Qazi, C. Chokshi, A. Ding, M. Subapanditha, N. Savage, S. Mahendram, E. Ford, A. A. Adile, D. McKenna, N. McFarlane, V. Huynh, R. G. Wylie, J. Pan, J. Bramson, K. Hope, J. Moffat, S. Singh, The rational development of CD133-targeting immunotherapies for glioblastoma. *Cell Stem Cell* **26**, 832–844 (2020).

58. J. Theruvath, E. Sotillo, C. W. Mount, C. M. Graef, A. Delaidelli, S. Heitzeneder, L. Labanieh, S. Dhingra, A. Leruste, R. G. Majzner, P. Xu, S. Mueller, D. W. Yecies, M. A. Finetti, D. Williamson, P. D. Johann, M. Kool, S. Pfister, M. Hasselblatt, M. C. Frühwald, O. Delattre, D. Surdez, F. Bourdeaut, S. Puget, S. Zaidi, S. S. Mitra, S. Cheshier, P. H. Sorensen, M. Monje, C. L. Mackall, Locoregionally administered B7-H3-targeted CAR T cells for treatment of atypical teratoid/rhabdoid tumors. *Nat. Med.* **26**, 712–719 (2020).

59. D. R. Spigel, H. Murthy, S. Chumsri, B. J. Ganguly, L. Gong, H. Hiraragi, E. Larsen, W. Liu, L. Martell, S. Zhu, I.-M. Bornman, S. Fitzsimmons, E. Barnum, S. Christiansen, H. Gillenwater, 777TiP Phase I study of LYL797, a ROR1-targeted CAR T-cell therapy with genetic and epigenetic reprogramming for the treatment of advanced solid tumors. *Ann. Oncol.* **33**, S896 (2022).

60. S. A. Oh, M. O. Li, TGF-β: Guardian of T cell function. *J. Immunol.* **191**, 3973–3979 (2013).

61. D. Padua, X. H. F. Zhang, Q. Wang, C. Nadal, W. L. Gerald, R. R. Gomis, J. Massagué, TGFβ primes breast tumors for lung metastasis seeding through angiopoietin-like 4. *Cell* **133**, 66–77 (2008).

62. M. Bose, P. Grover, A. J. Sanders, R. Zhou, M. Ahmad, S. Shwartz, P. Lala, S. Nath, M. Yazdanifar, C. Brouwer, P. Mukherjee, Overexpression of muc1 induces non-canonical tgf-β signaling in pancreatic ductal adenocarcinoma. *Front. Cell Dev. Biol.* **10**, 821875 (2022).

63. T. Tsukazaki, T. A. Chiang, A. F. Davison, L. Attisano, J. L. Wrana, SARA, a FYVE domain protein that recruits Smad2 to the TGFβ receptor. *Cell* **95**, 779–791 (1998).

64. N. Tang, C. Cheng, X. Zhang, M. Qiao, N. Li, W. Mu, X.-F. Wei, W. Han, H. Wang, TGF-β inhibition via CRISPR promotes the long-term efficacy of CAR T cells against solid tumors. *JCI Insight* **5**, e133977 (2020).

65. C. Bamdad, A. K. Stewart, B. J. Smagghe, P. Huang, N. D. Glennie, L. T. Deary, Novel CAR T that targets MUC1* not full-length MUC1 for treatment of solid tumor cancers. *Cytotherapy* **20**, S7 (2018).

66. J. Taylor-Papadimitriou, J. M. Burchell, R. Graham, R. Beatson, Latest developments in MUC1 immunotherapy. *Biochem. Soc. Trans.* **46**, 659–668 (2018).

67. J. Maher, S. Wilkie, D. M. Davies, S. Arif, G. Picco, S. Julien, J. Foster, J. Burchell, J. Taylor-Papadimitriou, Targeting tumor-associated glycoforms of MUC1 with CAR T cells. *Immunity* **45**, 945–946 (2016).

68. Y. Lin, S. Chen, S. Zhong, H. An, H. Yin, E. McGowan, Phase I clinical trial of PD-1 knockout anti-MUC1 CAR-T cells in the treatment of patients with non-small cell lung cancer. *Ann. Oncol.* **30**, xi12 (2019).

69. S. Depil, P. Duchateau, S. A. Grupp, G. Mufti, L. Poirot, 'Off-the-shelf' allogeneic CAR T cells: Development and challenges. *Nat. Rev. Drug Discov.* **19**, 185–199 (2020).

70. A. D. Posey Jr., R. D. Schwab, A. C. Boesteanu, C. Steentoft, U. Mandel, B. Engels, J. D. Stone, T. D. Madsen, K. Schreiber, K. M. Haines, A. P. Cogdill, T. J. Chen, D. Song, J. Scholler, D. M. Kranz, M. D. Feldman, R. Young, B. Keith, H. Schreiber, H. Clausen, L. A. Johnson, C. H. June, Engineered CAR T cells targeting the cancer-associated Tn-glycoform of the membrane mucin MUC1 control adenocarcinoma. *Immunity* **44**, 1444–1454 (2016).

71. R. Zhou, M. Yazdanifar, L. D. Roy, L. M. Whilding, A. Gavrill, J. Maher, P. Mukherjee, CAR T cells targeting the tumor MUC1 glycoprotein reduce triple-negative breast cancer growth. *Front. Immunol.* **10**, 1149 (2019).

72. M. K. Johnson, J. Korleski, A. Johnson, S. Sall, J. Laterra, H. Lopez-Bertoni, Abstract 5009: Inhibition of TGFBR2 signaling re-sensitizes TMZ-resistant glioblastoma cells to therapy. *Cancer Res.* **83**, 5009 (2023).

73. N. Zhang, M. J. Bevan, TGF-β signaling to T cells inhibits autoimmunity during lymphopenia-driven proliferation. *Nat. Immunol.* **13**, 667–673 (2012).

74. D. V. F. Tauriello, E. Sancho, E. Batlle, Overcoming TGFβ-mediated immune evasion in cancer. *Nat. Rev. Cancer* **22**, 25–44 (2022).

75. V. Narayan, J. S. Barber-Rotenberg, I.-Y. Jung, S. F. Lacey, A. J. Rech, M. M. Davis, W.-T. Hwang, P. Lal, E. L. Carpenter, S. L. Maude, G. Plesa, N. Vapiwala, A. Chew, M. Moniak, R. A. Sebro, M. D. Farwell, A. Marshall, J. Gilmore, L. Lledo, K. Dengel, S. E. Church, T. D. Hether, J. Xu, M. Gohil, T. H. Buckingham, S. S. Yee, V. E. Gonzalez, I. Kulikovskaya,

F. Chen, L. Tian, K. Tien, W. Gladney, C. L. Nobles, H. E. Raymond, D. Frazee, M. Truran, E. Veloso, H. McConville, J. Aguedelo, S. Hower, S. Ngo, J. Jadlowsky, J. J. Melenhorst, A. Roche, J. Everett, M. Gupta, F. Nazimuddin, C. Bartoszek, N. Koterba, R. Reynolds, F. Ellington, C. C. Kloss, J. Lee, Y. Zhao, J. Scholler, J. L. Riley, C. Bailey, A. White, B. Hudson, P. Chang, M. V. Maus, B. L. Levine, E. O. Hexner, D. L. Siegel, F. D. Bushman, C. H. June, J. A. Fraietta, N. B. Haas, PSMA-targeting TGFβ-insensitive armored CAR T cells in metastatic castration-resistant prostate cancer: A phase 1 trial. *Nat. Med.* **28**, 724–734 (2022).

76. M. Yi, T. Li, M. Niu, Y. Wu, Z. Zhao, K. Wu, TGF-β: A novel predictor and target for anti-PD-1/PD-L1 therapy. *Front. Immunol.* **13**, 1061394 (2022).

77. S. Bao, X. Jiang, S. Jin, P. Tu, J. Lu, TGF-β1 induces immune escape by enhancing PD-1 and CTLA-4 expression on T lymphocytes in hepatocellular carcinoma. *Front. Oncol.* **11**, 694145 (2021).

78. E. Meulmeester, P. Ten Dijke, The dynamic roles of TGF-β in cancer. *J. Pathol.* **223**, 205–218 (2011).

79. B. Aranda-Orgilles, I. Chion-Sotinel, J. Skinner, S. Grudman, B. Mumford, C. Dixon, J. P. Fernandez, P. Erler, P. Duchateau, A. Gouble, R. Galetto, L. Poirot, Preclinical evidence of an allogeneic dual CD20xCD22 CAR to target a broad spectrum of patients with B-cell malignancies. *Cancer Immunol. Res.* **11**, 946–961 (2023).